

Loop Current Ring Shedding: The Formation of Cyclones and the Effect of Topography

LAURENT M. CHÉRUBIN

Division of Meteorology and Physical Oceanography, Rosenstiel School of Marine and Atmospheric Science, University of Miami, Miami, Florida

YVES MOREL

LEGOS/Service Hydrographique et Océanographique de la Marine, Toulouse, France

ERIC P. CHASSIGNET

Division of Meteorology and Physical Oceanography, Rosenstiel School of Marine and Atmospheric Science, University of Miami, Miami, Florida

(Manuscript received 31 January 2005, in final form 7 September 2005)

ABSTRACT

The formation of cyclones in the vicinity of the Loop Current ring during the separation stage is analyzed in the frame of a high-resolution ECMWF daily wind-forced Miami Isopycnic Coordinate Ocean Model (MICOM) simulation. Mesoscale cyclones, observed in sea surface height maps in the vicinity of the Loop Current in a necking-down position, are found to contribute to the separation of the ring from the Loop Current as they grow between the Loop Current and the ring in the MICOM simulation. To understand the origin of the cyclones, the instability of the Loop Current idealized as an isolated vortex is studied. After noticing the cyclonic vorticity belt around the Loop Current, and based on the vertical distribution of potential vorticity in a Loop Current ring in the MICOM simulation, the linear stability of a shielded vortex is studied in the quasigeostrophic formalism. To simulate the effects of the planetary vorticity gradient and topography on the Loop Current, the nonlinear states of the idealized Loop Current are analyzed using the adiabatic MICOM code. Results from the analysis of the MICOM simulation show that cyclones are the products of a vortex rim instability. The modal analysis of the Loop Current instability reveals that mode 4 is the fastest-growing mode and that baroclinic (barotropic) instability is intensified in the deep (surface) layers. These results are confirmed by the analytical study of the idealized Loop Current. The nonlinear state shows that a Loop Current-like vortex is indeed a pentapole on an f plane. On the β plane, the northern cyclone is separated from the anticyclone by the β effect and both drift westward. When the topography of the Gulf of Mexico is taken into account—namely, the Campeche Bank, the southward slope north of the Loop Current, and the Florida shelf east of the Loop Current—several effects are observed: 1) the northern corner of the Campeche Bank erodes the Loop Current ring and its cyclones and interacts with the vortex's most unstable mode, 2) the northern southward slope scatters the northern cyclone while the anticyclone remains coherent and propagates to the west, and 3) realistic westward propagation speeds are obtained in the presence of the northern Campeche shelf, which acts as a mirror effect on the Loop Current ring, as opposed to the Florida shelf, which tends to block the ring.

1. Introduction

The Gulf of Mexico is a semienclosed sea connected to the Caribbean Sea by the Yucatan Channel. The

Caribbean Sea carries into the Gulf of Mexico the influence of the western branch of the North Atlantic Ocean subtropical gyre. The waters of the Caribbean enter the Gulf of Mexico as an intense jet called the Yucatan Current. As the current propagates northward, leaving the channel and spreading in the southeastern part of the Gulf, it forms the pulsating Loop Current. Finally, the Loop Current leaves the Gulf of Mexico through the Florida Straits, originating the

Corresponding author address: Laurent Chérubin, RSMAS-MPO, University of Miami, 4600 Rickenbacker Cswy., Miami, FL 33149.
E-mail: lcherubin@rsmas.miami.edu

Florida Current, which in turn becomes the Gulf Stream.

Two remarkable processes associated with the Loop Current have been extensively studied—namely, its extensive northward migration onto the northeastern Gulf of Mexico continental shelf and the associated shedding of mesoscale anticyclonic rings called Loop Current rings. The process of separation of warm-core or anticyclonic rings from the Loop Current [originally suggested by Ichiye (1962)] is considered by some to be the most intriguing large-scale physical process occurring in the Gulf of Mexico. The mechanism of separation of warm-core rings from the Loop Current was first examined in detail by Hurlburt and Thompson (1980, 1982) using numerical model results. In their two-layer model, they focused on the role of barotropic instability fed by the upper-layer kinetic energy when the Loop Current ring pinches off. During the interval between eddy shedding, the model Loop Current did not always meet the necessary instability criterion, so that ring formation time was not determined by an instability growth rate but rather by the time required for the Loop Current to penetrate into the Gulf and bend to an unstable configuration, at which time an instability grows very rapidly. They found that their model lower-layer flow in the vicinity of the Loop Current ring was characterized by a deep cyclone–anticyclone pair, a feature also present in other numerical experiments (Sturges et al. 1993; Welsh 1996; Inoue 1998; Welsh and Inoue 2000).

Surface cyclonic rings are also observed in the Gulf of Mexico. Cochrane (1972) was the first to propose that Loop Current rings could be separated from the Loop Current by cyclonic rings. Elliot (1979) suggested that cyclones observed in the western Gulf were formed along the Loop Current in the eastern Gulf and propagated into the western Gulf during the formation of a Loop Current ring. This scenario was expanded by Vukovich et al. (1979) and Vukovich and Maul (1985). The latter authors speculated that the cold features (the cyclones) intensify through instability processes, thereby leading to the formation below the surface layer of an anticyclone, which then leads to the westward propagation of the cold features in the shear zone between the ring and the Loop Current to the south.

Cyclones were also found to play a role in the separation process in numerical experiments (Hurlburt 1985, 1986; Wallcraft 1985, 1986; Oey 1996). Eddies or meanders were observed to form on the cyclonic shear side of the Loop Current, southwest of its center, and propagate around the loop. In Hurlburt (1985, 1986), some cyclones nearly reached the outflow port (entrance of the Florida Straits), traveling at 15 km day^{-1} ,

similar to the observational results of Vukovich et al. (1979) and Vukovich and Maul (1985). These cyclonic eddies were formed about every 20 days, but only during a few months prior to an eddy-shedding event. In Oey (1996), these cyclones appear to play a role in Loop Current ring separation (see his Fig. 5). However, Oey (1996), as well as Hurlburt and Thompson (1982) and Sturges et al. (1993), also found Loop Current ring separation without resolving Loop Current ring cyclones in their numerical models.

Satellite data have confirmed the existence of these cyclonic features (also called frontal eddies) along the boundary of a warm-core ring. Figure 1 is an example of sea surface height (SSH) maps based on satellite altimetry (Biggs et al. 1996) that show the Loop Current in necking-down position surrounded by three cyclones (blue indicates the lowest sea surface heights). Fratantoni et al. (1998) showed from their observations that Loop Current frontal cyclones are found not only before a ring shedding, but also during the entire extension process. Schmitz (2003) surmised that these frontal eddies may originate from an instability process and possibly amplify and play a role in ring separation.

Using a European Centre for Medium-Range Weather Forecasts (ECMWF) daily forced very high resolution Miami Isopycnic Coordinate Ocean Model (MICOM) numerical simulation of the Atlantic Basin, Chérubin et al. (2005) observed the generation of strong deep currents underneath the Loop Current ring, preceding its separation from the Loop Current. These deep current bursts were shown to be the product of the growth of an instability in the deep part of the Loop Current ring before separation. The vortex instability then produced three or four cyclones at the rim of the anticyclonic core (Fig. 2). The cyclones then grow between the Loop Current and the Loop Current ring (Figs. 2c and 2d) and, thus, contribute to the separation of the Loop Current ring from the Loop Current. Most likely, the Loop Current ring interacts with the topography during the separation process and the westward propagation. To understand the origin of the cyclones, we study in this paper the instability of the Loop Current idealized as an isolated vortex. Based on the vertical distribution of potential vorticity in a Loop Current ring in the MICOM simulation, the linear stability of a shielded vortex (the anticyclonic core is surrounded by a cyclonic belt) is studied in the quasigeostrophic (QG) formalism. To simulate the effects of the planetary vorticity gradient and topography on the Loop Current, the nonlinear states of the idealized Loop Current are analyzed using the adiabatic MICOM code.

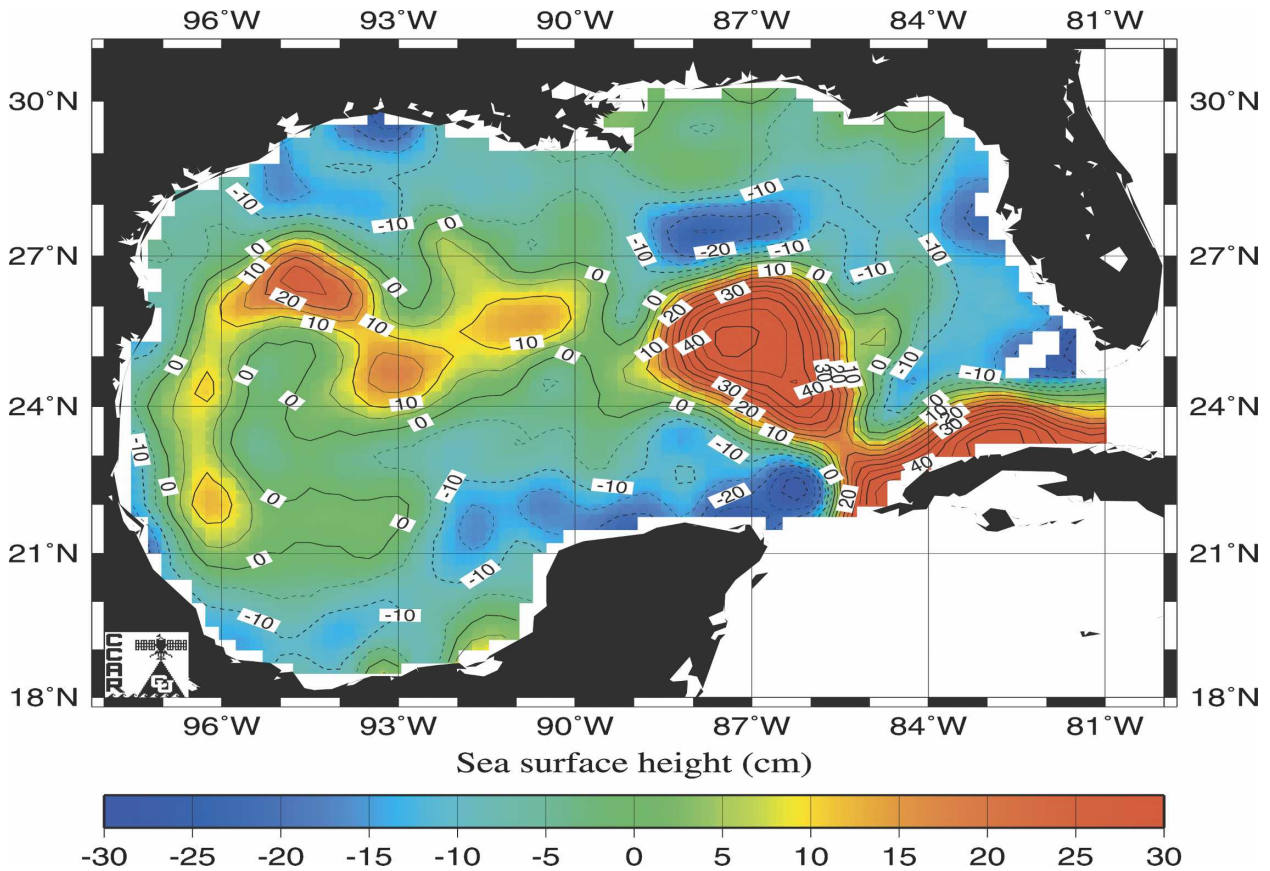


FIG. 1. SSH (15 Aug 1996) map of the Gulf of Mexico from the Real-Time Altimetry project at the Colorado Center for Astrodynamics Research. Blue (red) indicates the lowest (highest) sea level.

The paper is organized as follows: in section 2, we examine the characteristics of the instability of the Loop Current during a shedding event in the ECMWF-forced MICOM simulation, and we build a simplified model (by reducing the number of layers) of the Loop Current. In sections 3 and 4, we study the stability and the nonlinear regimes of the idealized anticyclonic-shielded vortex, and we focus on the influence of β and topography on the most unstable normal mode perturbation. Both β and the topography strongly perturb the nonlinear vortex behavior and the generation of cyclones. We also investigate their reciprocal effect on the nonlinear regimes. Conclusions are drawn in section 5.

2. Characteristics of the instability of the Loop Current rings in the MICOM simulation

This section builds upon a very high resolution ($1/12^\circ$) North Atlantic MICOM simulation that exhibits a realistic circulation in the Gulf of Mexico (Garraffo et al. 2001; Chassignet and Garraffo 2001; Romanou et al. 2004; Chérubin et al. 2005). MICOM reproduces the

most important characteristics of flow in the Caribbean Sea, the Yucatan Channel, and the Gulf of Mexico (see Chérubin et al. 2005 for detail). After a brief description of the numerical simulation, the Loop Current ring-shedding process is analyzed in terms of potential vorticity anomaly and energy transfers.

a. ECMWF daily forced $1/12^\circ$ MICOM simulation

The fundamental reason for modeling ocean flow in density (isopycnic) coordinates, as in MICOM, is that this system suppresses the diapycnal component of numerically caused dispersion of material and thermodynamic properties (temperature, salinity, etc.) and allows the user to prescribe/parameterize the diapycnal physical processes. This allows isopycnic models to preserve their water mass characteristics and prevents the warming of deep water masses that has been shown to occur in models framed in Cartesian coordinates (Chassignet et al. 1996). The computational domain is the North and equatorial Atlantic Ocean basin from 28°S to 70°N , including the Caribbean Sea, the Gulf of Mexico, and the Mediterranean Sea. The horizon-

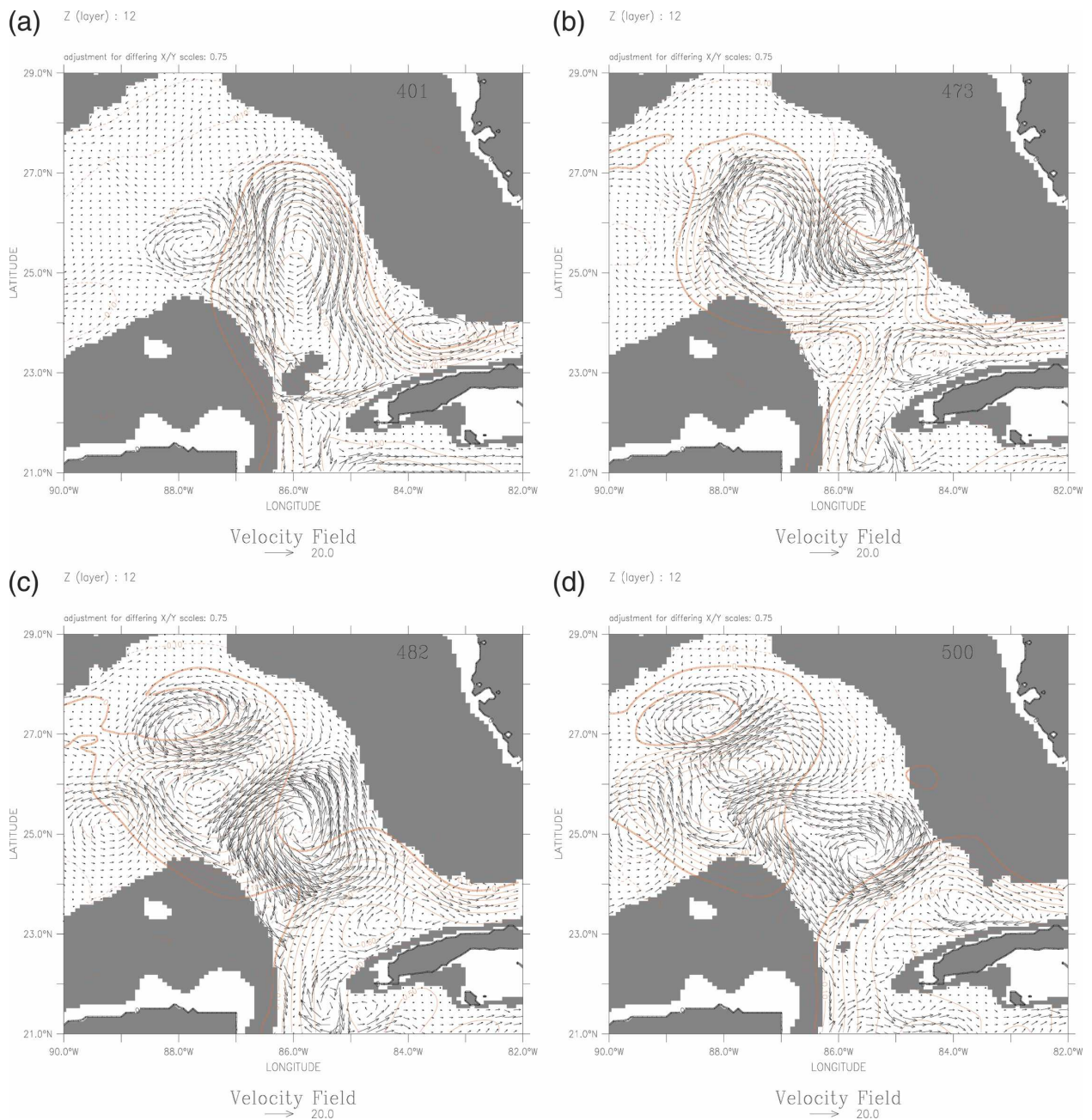
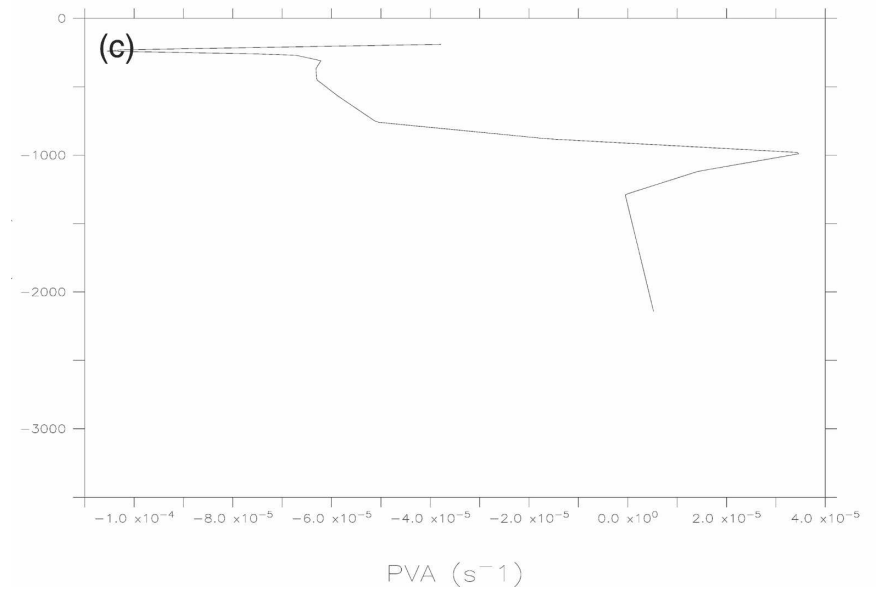
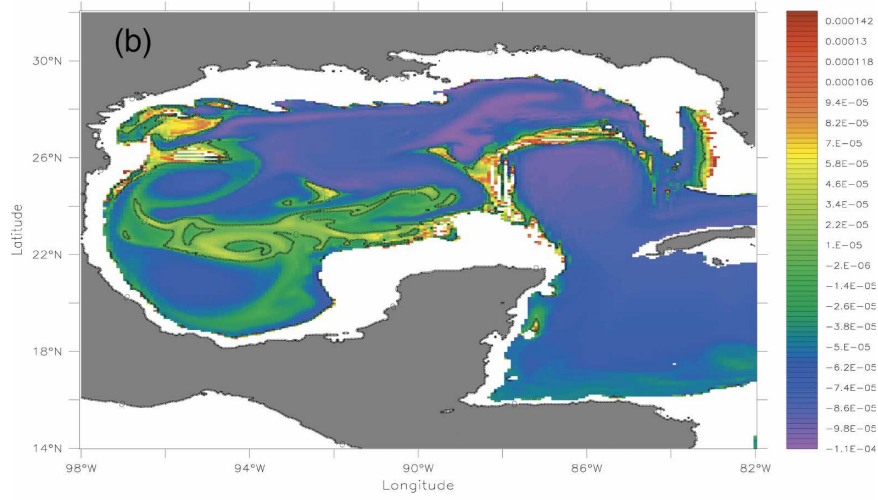
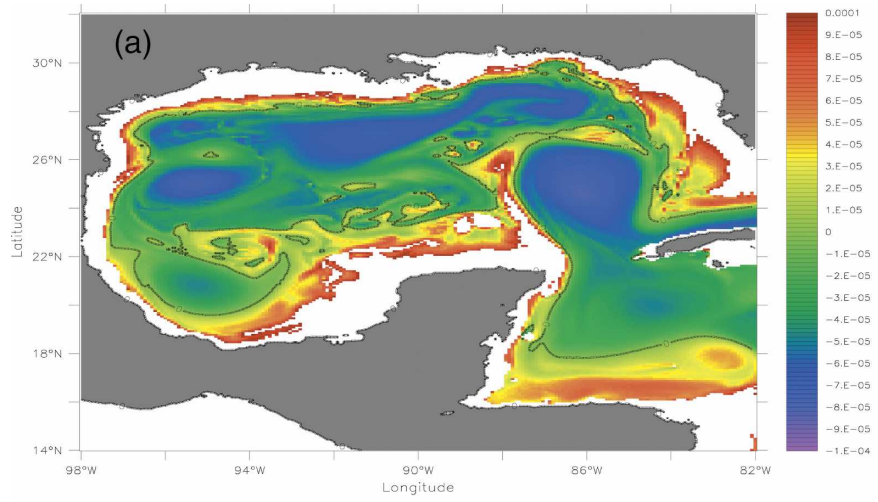


FIG. 2. (a)–(d) Frame sequence of the flow circulation in MICOM layer 12 superimposed on the SSH (red contours; m). Solid lines are positive contours. The gray shading corresponds to the bottom topography mask. The number in each frame is the day. The scale (cm s^{-1}) of the arrows is given by the vector length just below the frame (from Chérubin et al. 2005).

→

FIG. 3. Maps of the potential vorticity anomaly in the MICOM North Atlantic high-resolution simulation before the Loop Current ring-shedding event. Violet (red) indicates strong negative (positive) anomalies. The black contour shows the change of sign of the potential vorticity anomaly: (a) layer 1 (≈ 50 m deep) of the model and (b) layer 4 (≈ 200 m deep). (c) The potential vorticity anomaly vertical profile in the core of the Loop Current ring.



tal grid (6 km on average) is defined on a Mercator projection with resolution given by $1/12^\circ \times 1/12^\circ \cos(\phi)$, where ϕ is the latitude. The bottom topography is derived from a digital terrain dataset with 5' latitude–longitude resolution (5' Gridded Earth Topography data: ETOPO5). The vertical density structure is represented by 19 isopycnic layers topped by an active surface mixed layer that exchanges mass and properties with the isopycnic layers underneath. The vertical discretization was chosen to provide maximum resolution in the upper part of the ocean. Open-ocean boundaries are treated as closed but are outfitted with 3° buffer zones in which temperature (T) and salinity (S) are linearly relaxed toward their seasonally varying climatological values (Levitus 1982), with damping/relaxation times from 5 days at the wall to 30 days at the inner edge of the buffer zone. These buffer zones restore the T and S fields to climatology in order to approximately recover the vertical shear of the currents through geostrophic adjustment. After a 6-yr spinup with monthly climatological forcing, the model was integrated using surface boundary conditions based on ECMWF daily atmospheric data from 1979 to 1986. The diapycnal mixing consists of a background value of $1 \text{ cm}^2 \text{ s}^{-1}$ and a Richardson number–dependent entrainment parameterization (Papadakis et al. 2003). The high horizontal grid resolution dramatically improved the model's behavior in comparison with that of previous coarse-resolution simulations. The major improvements are an excellent representation of western boundary currents (surface and deep) including a correct Gulf Stream separation (Chassignet and Garraffo 2001) as well as higher eddy activity (Paiva et al. 1999). As mentioned above, the modeled Florida Straits transport is on average $31.4 \times 10^6 \text{ m}^3 \text{ s}^{-1}$ (transport information available online at <http://oceanmodeling.rsmas.miami.edu/micom>), in line with observations.

b. Potential vorticity variations in the Loop Current

We analyze here the potential vorticity anomaly changes of the Loop Current during a ring formation in the MICOM simulation. In the absence of dissipative effects, for each isopycnal layer, potential vorticity is conserved for each particle of the flow (Ertel 1942; Pedlosky 1987) and can be written as

$$\text{PV} = \frac{\zeta + f}{h}, \quad (1)$$

where $\zeta = \partial_x v - \partial_y u$ is the relative vorticity, h is the thickness of an isopycnal layer, and f is the Coriolis frequency. It is also useful to define another quantity that we will refer to as the equivalent quasigeostrophic

potential vorticity anomaly (PVA; see Herbette et al. 2003):

$$\begin{aligned} \text{PVA} &= H \left(\frac{\zeta + f}{h} - \frac{f}{H} \right) \\ &= \frac{H}{h} \left[\zeta - \frac{f(h - H)}{H} \right], \end{aligned} \quad (2)$$

where H is constant and represents the unperturbed layer thickness. By removing the ambient potential vorticity, the potential vorticity gradients are more clearly seen, therefore facilitating the study of baroclinic and barotropic instabilities that owe their existence to these potential vorticity gradients (Hoskins et al. 1985). In the MICOM simulation, H is provided by the thickness of the layer in the far field from the Loop Current area, which we choose to be west of the Campeche Bank where the disturbance activity is less than elsewhere in the Gulf of Mexico. Layer-by-layer maps of the potential vorticity anomaly were computed in the Gulf of Mexico relative to this area. PVAs in layer 1 and 4 are displayed in Fig. 3 during the northward extension process of the Loop Current. These show that the Loop Current ring is in part surrounded by a belt of positive PVA both at the surface and at depth.

Figure 3a shows that, at the surface layer, the core of the Loop Current has a strong negative potential vorticity anomaly ($\approx -9 \times 10^{-5} \text{ s}^{-1}$). This core is embedded in a belt of less strong potential vorticity anomaly ($\approx -6.5 \times 10^{-5} \text{ s}^{-1}$) surrounded by another belt of positive potential vorticity anomaly. This belt is eventually surrounded by flows of negative potential vorticity anomaly ($\approx -10 \times 10^{-5} \text{ s}^{-1}$). The Charney–Stern theorem (Charney and Stern 1962) stipulates that the potential vorticity gradients must change sign in or between layers for barotropic or baroclinic instability, respectively, to exist. Therefore, the horizontal distribution of the potential vorticity anomaly in the Loop Current (also observed at depth; Fig. 3b) provides the necessary condition for barotropic instability. In the vertical, the PVA of the core of the Loop Current ring changes sign near 1000 m, as shown in Fig. 3c, also indicating that the necessary condition for baroclinic instability is satisfied.

We now further analyze the connection between the change of sign of the layerwise PVA and the Loop Current behavior. To provide a picture of the evolution of the PVA in the Loop Current during the formation of Loop Current rings, we show in Fig. 4 the time series of the potential vorticity anomalies in layers 2, 6, and 12 during six ring formation events in the MICOM simulation. Each formation period, called a cycle, starts and

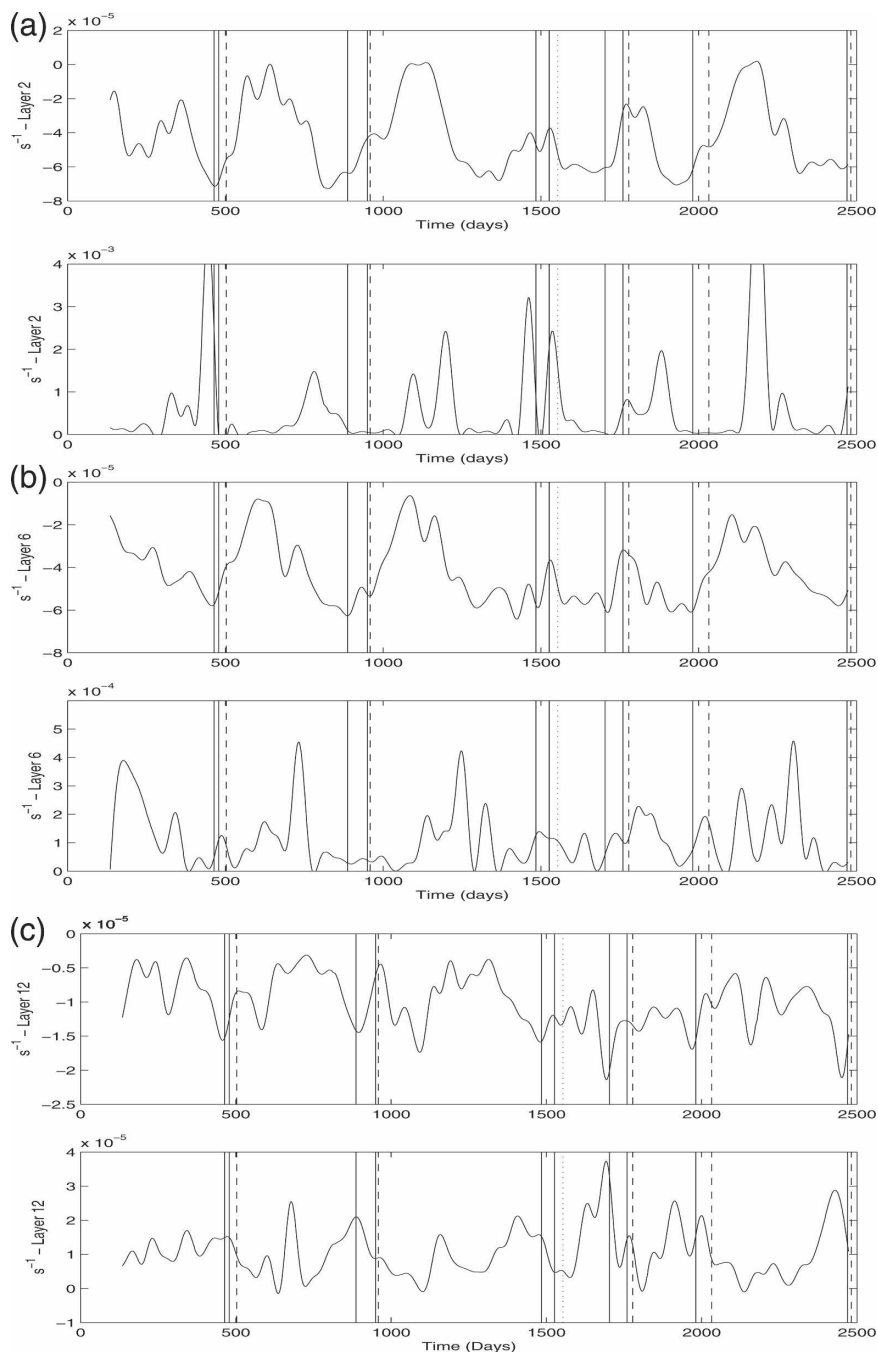


FIG. 4. Time series of potential vorticity anomalies from the MICOM North Atlantic high-resolution simulation: (a) layer 2 (≈ 150 m deep), (b) layer 6 (≈ 350 m deep), and (c) layer 12 (≈ 1000 m deep). These time series cover the six integral ring-shedding events and are series of the zonal average, at 25°N and between $88^\circ30'$ and $83^\circ30'\text{W}$, of (top panels) negative and (bottom panels) positive potential vorticity anomalies across the Loop Current. Each separation is marked by a vertical solid line. Two solid lines indicate that the Loop Current ring reattaches between the separations. The dashed line marks the end of the cycle, the return of the Loop Current to its port-to-port configuration.

ends at a dashed line, which marks the end of the separation process as visually observed. For each layer displayed, the time series compared two plots. The top (bottom) panel of Fig. 4 displays the zonal average across the Loop Current, at 25°N and between 88°30' and 83°30'W, of negative (positive) PVA time series. Negative PVA represents the core of the Loop Current ring, and positive PVA the belt. In the three layers displayed, each shedding event is preceded by a long period of high negative potential vorticity anomaly. Similarly, the shedding events are also preceded by the sudden increase in positive potential vorticity anomaly, at the end of the negative potential vorticity anomaly period. The shedding events are therefore dependent on the potential vorticity gradient across the Loop Current. It is worth noting in layer 2 that at the end of the third cycle, the slight decrease of negative PVA is associated with the failure of the shedding. The Loop Current ring reattached to the Loop Current.

These results compare well with the observations of Candela et al. (2002) obtained from current measurements in the Yucatan Channel during the CANEK¹ experiment (Ochoa et al. 2001). Indeed, during a period of negative vorticity influx, the Loop Current tends to grow in extension, in area, or in both. During periods of positive influx, the Loop Current retracts and a ring can be shed.

c. Energy transfer analysis

To assess the nature of the instabilities and where in the water column they take place, we analyze here the energy transfer time series during the six ring-shedding cycles. Hurlburt and Thompson (1982) first showed that barotropic instability was responsible for ring formation in a flat-bottom two-layer model. Decreasing the horizontal viscosity of the numerical model in comparison with that of the Hurlburt and Thompson's (1982) model, Hurlburt (1985, 1986) analyzed numerical model results for the Gulf of Mexico in which cy-

clonic frontal eddies were present at the rim of the Loop Current. Hurlburt (1985, 1986) found that the Loop Current shedding process was connected with a mixed barotropic–baroclinic instability.

In the MICOM simulation, the eddy kinetic and potential energy and the two energy transfers are computed in a box comprising the growing and shedding areas of the Loop Current for the six formation cycles. The box latitude ranges from 23° to 29°N and its longitude ranges from 91° to 83°W. The box-average eddy kinetic energy and the transfer terms are calculated as expressed by Bleck (1985) and Chassignet and Boudra (1988). The eddy kinetic energy is computed from the difference between the in situ and the time-averaged velocity fields. The layerwise transfers of energy from the mean to the disturbance flow are $C(P, K_E)$, the baroclinic conversion, and $C(K_M, K_E)$, the barotropic conversion. Figure 5a shows that the eddy kinetic energy and the potential energy of the perturbation increase just before the shedding events. Figure 5b shows that the baroclinic conversion is toward the mean flow during the Loop Current ring growth (<0) and then toward the eddy field during the shedding event (>0). The baroclinic conversion is enhanced in the deep layers of the Loop Current ring. The transfer of kinetic energy from the mean flow to the perturbation increases near the shedding event and decreases in magnitude from layer 1 to layer 9 (Fig. 5c). Overall, baroclinic (barotropic) instability is intensified in the deep (upper) layers of the Loop Current. This result confirms that the shedding events in the MICOM simulation are driven by instabilities and that both baroclinic and barotropic instabilities play a significant role in the separation of the Loop Current ring, in agreement with the results of Hurlburt (1985, 1986). In the following section, we will show that the unstable behavior of an idealized Loop Current ring model based on the MICOM horizontal and vertical PVA distribution leads to the formation of cyclones that grow between the ring and the Loop Current (Fig. 2).

3. Instability properties of a shielded vortex on a flat bottom

The horizontal and vertical PVA distribution in the modeled Loop Current and in its vicinity (as described in section 2) are used in this section to build an analytical model aimed at studying the instability of a Loop Current ring-like vortex. The horizontal and vertical distribution of the PVA is modeled as shown in Fig. 6, with the spatial PVA structure of the Loop Current taken into account. This figure shows a vertical cross section of the Loop Current ring model built upon strip-wise constant PVA that will be used for the QG

¹ The CANEK project was initiated in December 1996 with the main objective of measuring the exchange flow between the Gulf of Mexico and the Caribbean Sea through the Yucatan Channel. Six cruises were successfully concluded: December 1996, May 1997, March 1998, January 1999, August 1999, and June 2000. During these cruises extensive shipboard ADCP and CTD/LADCP surveys of the region were carried out. In August 1999, an eight-mooring array, containing 33 Aanderaa current meters and eight upward-looking ADCPs, was deployed across the Yucatan Channel, fully recovered in June 2000, and redeployed for final recovery on June 2001. This research was supported by Centro de Investigacion Cientifica y de Educacion Superior de Ensenada (CICESE), Mexico Rs CONACyT, and the Inter-Americas Institute for Global Change (IAI), and through contracts with Deepstar.

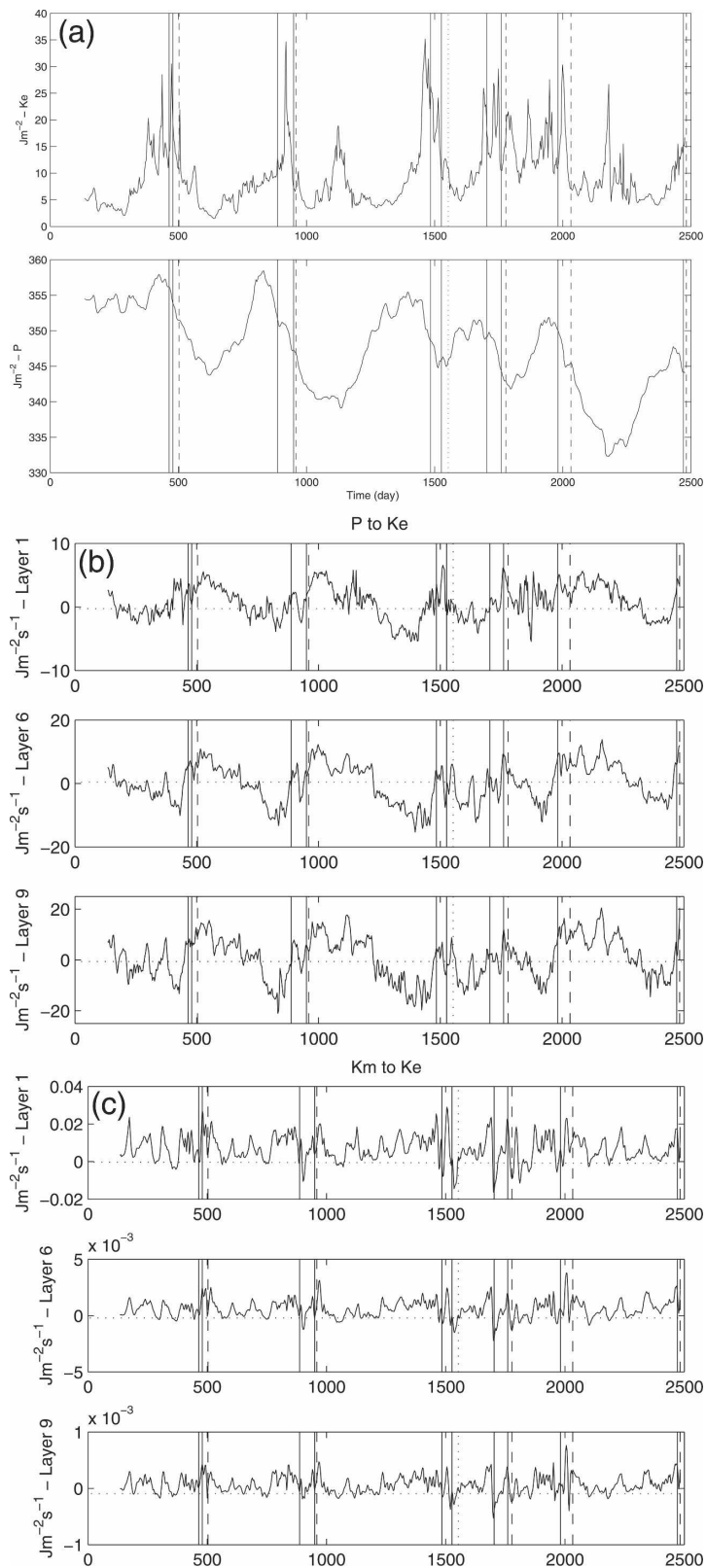


FIG. 5. (a) Time series of the (top) eddy kinetic energy and (bottom) potential energy from the MICOM simulation. (b) The baroclinic conversion term $C(P, K_E)$ for (from top to bottom) layers 1 (≈ 50 m deep), 6 (≈ 350 m deep), and 9 (≈ 700 m deep). (c) The barotropic conversion $C(K_M, K_E)$ for the same layers as in (b).

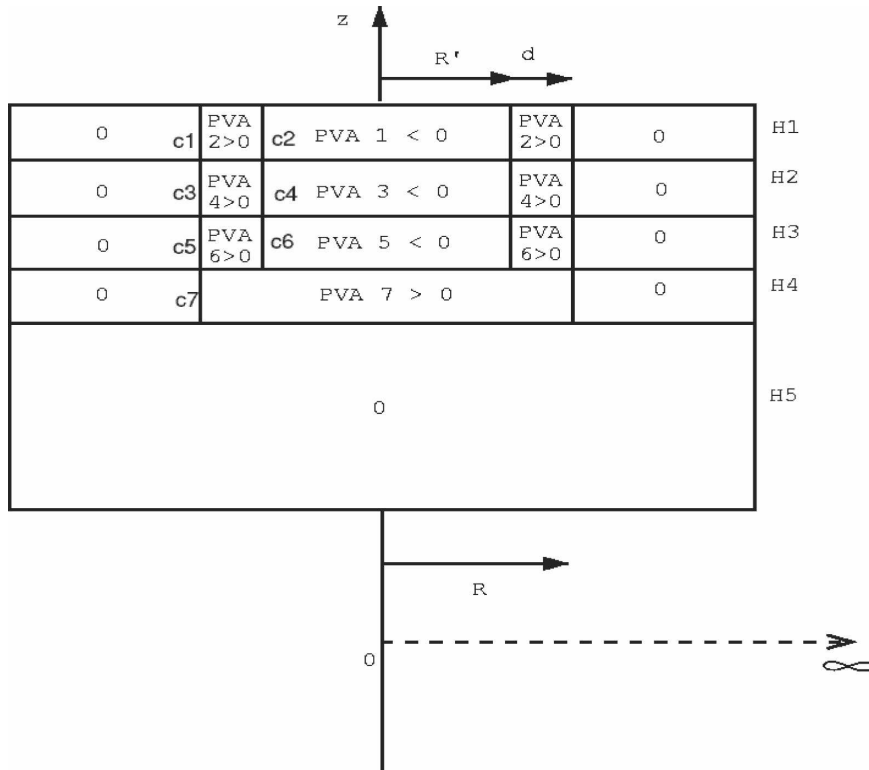


FIG. 6. Cross section of the QG Loop Current ring model used for the analytical study. Two circular PVA contours are defined per layer in the first three layers. The inner (outer) contour is around the anticyclonic (cyclonic) core (belt). Only one circular contour is defined in layer 4. PVA contours are labeled c_j , where j is the contour number, R is the vortex radius defined here by the external rim of the cyclonic belt, d is the width of the cyclonic belt, R' is the radius of the inner core, and H_i , $i = 1-5$, is the layer thickness.

instability study. In the first three layers, the anticyclonic core is surrounded by a cyclonic PVA belt. Based on the vertical PVA profile, the fourth layer of the vortex has a cyclonic PVA. The fifth layer has an infinite depth and no PVA. This type of vortex is called a shielded ring, and its linear and nonlinear stability are studied in the remainder of this section. Both barotropic and baroclinic instabilities can exist within this idealized vortex in accordance with the Charney–Stern criteria. Impacts of the β effect and topography are studied in section 4.

a. Linear instability

To analytically derive the growth rates associated with the above shielded vortex, we need to define an initial PVA profile so that the vortex is isolated and the QG approximation is satisfied. A necessary and sufficient condition for a vortex to be isolated is that the area integral of the relative vorticity ($\zeta = \partial_x v - \partial_y u = \nabla^2 \psi$) vanishes at all depths (Flierl 1987):

$$\iint \zeta(x, y, z) dx dy = 0. \quad (3)$$

This condition is generally satisfied by the Loop Current ring at the beginning of the shedding process when the anticyclonic core is partially surrounded by a cyclonic belt. To ensure the vortex is isolated in our analytical model, we use a continuous-power exponential radial profile and annular shielding in the PVA for the first three layers,

$$\text{PVA}_k = \Delta Q_k \left[1 - \frac{\alpha}{2} \left(\frac{r}{R} \right)^\alpha \right] \exp \left[- \left(\frac{r}{R} \right)^\alpha \right], \quad (4)$$

$k = 1, 2, 3,$

and a power exponential radial profile only in layer 4,

$$\text{PVA}_4 = \Delta Q_4 \exp \left[- \left(\frac{r}{R} \right)^\alpha \right], \quad (5)$$

where R is the radius of the vortex and ΔQ_k is the maximum PVA in each layer. These profiles are such that the total circulation is zero for any α in each layer (Carton and Legras 1994). The parameter α defines the width of the cyclonic belt. Large α corresponds to a narrow belt.

In the ECMWF daily forced MICOM simulation described in section 2, the maximum vortex azimuthal speed is $V = 1.5 \text{ cm s}^{-1}$, the vortex radius (outer rim of the cyclonic belt) is $R = 250 \text{ km}$ (see Fig. 6, or 200 km if R is the radius of maximum velocity), and the Coriolis parameter at its latitude is $f_0 = 4.2 \times 10^{-5} \text{ s}^{-1}$. This leads to the Rossby number $\text{Ro} = 0.14$. Using a density jump of $\Delta\rho/\rho = 6.8 \times 10^{-4}$, along with the thickness of the first two layers $H = 240 \text{ m}$, the Burger number is $\text{Bu} = 0.015$. Therefore, $\text{Ro}/\text{Bu} \gg 1$, which does not satisfy the quasigeostrophic approximation, as vertical deviations of the density interface are large for the mean vortex. However, Boss et al. (1996) showed that the quasigeostrophic framework is adequate for describing the instability of a PV front even in regimes where the quasigeostrophic assumptions are violated. Therefore, we investigate the Loop Current model stability with a $4\frac{1}{2}$ -layer quasigeostrophic analytical model made of piecewise constant strips of PVA. The agreement between the linear instability study results and the nonlinear results (section 3b) will confirm a posteriori this choice. Because the vortex core is surrounded by a ring of opposite sign PVA, we will refer to this vortex as an R vortex, following Morel and McWilliams's (1997) classification. The derivation of the analytical model is given in the appendix and we now study the idealized Loop Current stability.

The background stratification in the idealized vortex is defined from densities used in the MICOM simulation (numerical values are given in Table 1). The vortex radius is chosen to be $R = 250 \text{ km}$ (rim of the cyclonic belt) and the first internal radius is $R_d = 50 \text{ km}$. The idealized vortex is initialized with PVA profiles (4) and (5), which provide the potential vorticity anomaly jumps and their positions for the linear QG instability model. The vortex piecewise constant potential vorticity anomalies are chosen so that, in each layer, the initial axisymmetric velocity field has realistic extrema at the radius obtained from the MICOM simulation. Thus, the potential vorticity jumps in each layer are calculated from a reference PV jump $\Delta Q_0 = -4 \times 10^{-5} \text{ s}^{-1}$ (Table 1). The parameter α controls the horizontal shear between the anticyclonic core and the cyclonic belt, which is equivalent to specifying the width d (see

Fig. 6) of the shield. Flierl (1988), Carton and McWilliams (1989), Carton and Legras (1994), and Baey and Carton (2002), among others, showed the dependence of instability on the vorticity profile, controlled here by the steepness parameter α .

Figure 7a shows that mode $m = 4$ is the most unstable mode for this vortex and is triggered when $\alpha \geq 4$. This corresponds to a sufficiently small width of the shield or sufficiently strong horizontal shear. This result agrees with that of Flierl (1988), regarding the growth of high modes for narrow outer shear regions in a two-layer shielded vortex model. Figure 7b displays the amplitude of the deviation of the PVA fronts $\eta_{k,j}$ (see the appendix, and for the front numbering see Fig. 6). First, this diagram confirms the mixed nature of the vortex instability. Fronts in different layers are resonant (baroclinic instability) and fronts in the same layer are also resonant (barotropic instability). Second, Fig. 7b shows that baroclinic instability is bottom intensified (contours c5 and c7) while barotropic instability is surface intensified (contours c1 and c2). This vertical structure agrees with the results obtained in the MICOM simulation (see section 2). We also recover some important properties of shielded vortices found by Saunders (1973) and Flierl (1988), such as the effect of the ratio of the vortex scale to the Rossby radius of deformation. Figure 7c shows that large values of this ratio lead to higher-mode instabilities triggered in vortices with narrower outer shear regions. However, there is a parameter range for which the growth of instability is maximum.

b. Nonlinear evolution and multipoles stability

The nonlinear evolution of the idealized vortex described in section 3a is obtained using the adiabatic version of the MICOM model (Jacob et al. 2002; Herbert et al. 2003; Y. Morel 2001, unpublished manuscript). The numerical model is initialized with the same horizontal potential vorticity anomaly profiles as in the analytical study [see (4) and (5)].

The nonlinear steady state of the nonperturbed idealized vortex on an f plane, for $\alpha = 8$ in layers 1 and 3, is presented in Fig. 8. As predicted by the linear instability study, the mode $m = 4$ is the fastest-growing mode for $\alpha = 8$. A pentapole is formed and remains as a long-lived stable multipolar structure. The choice of α was guided by the compromise between realistic orthoradial velocities and the stability of the anticyclonic core alone after interaction with β and topography (section 4). Morel and Carton (1994) showed the existence of dipolar and tripolar stable equilibria for a two-contour Rankine vortex type in two-dimensional flows. But the stable pentapole obtained in this study shows that more complex multipoles, other than tripoles and quadru-

TABLE 1. Physical parameters of vortex model.

Layer	Layer thickness (m)	ρ (kg m^{-3})	ΔQ
1	$H_1 = 150$	$\rho_1 = 1023.81$	$\Delta Q_1 = 0.6\Delta Q_0$
2	$H_2 = 50$	$\rho_2 = 1025.06$	$\Delta Q_2 = \Delta Q_0$
3	$H_3 = 500$	$\rho_3 = 1025.64$	$\Delta Q_3 = 0.6\Delta Q_0$
4	$H_4 = 250$	$\rho_4 = 1026.05$	$\Delta Q_4 = -0.06\Delta Q_0$
5	$H_5 = 4000$	$\rho_5 = 1046.05$	$\Delta Q_5 = 0$

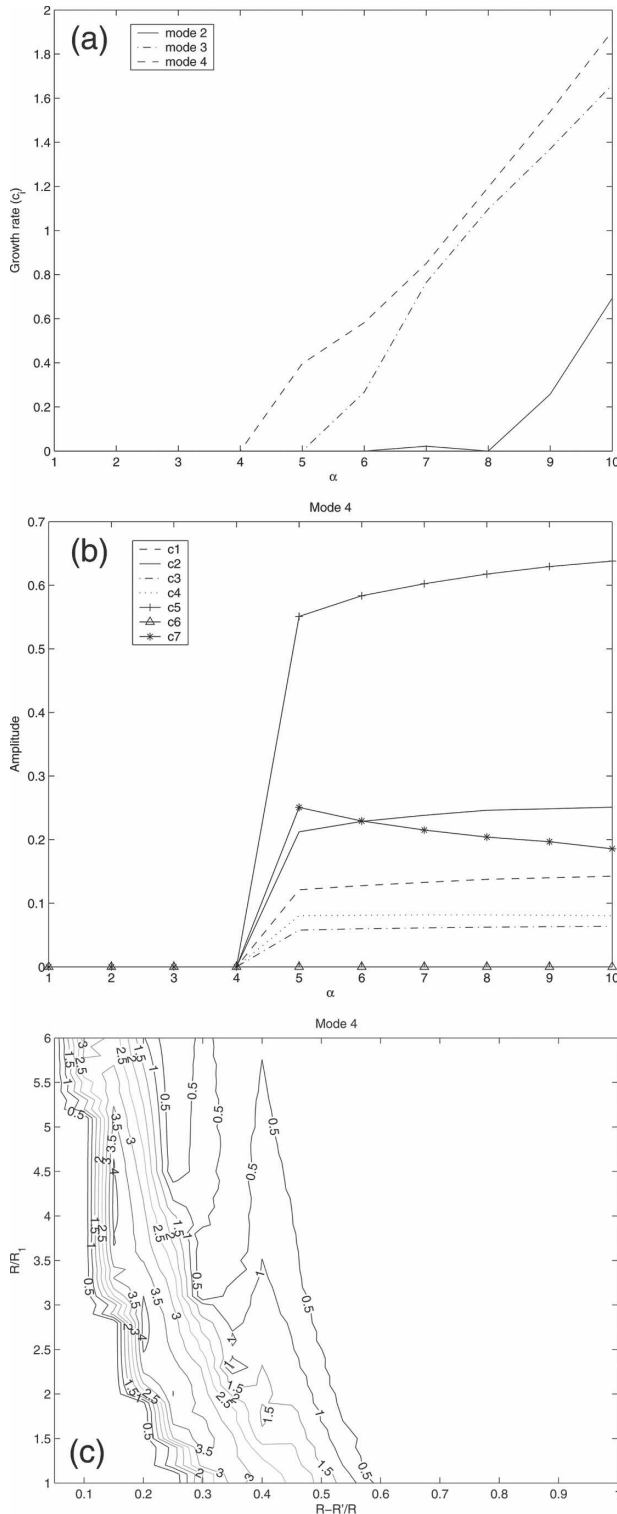


FIG. 7. (a) Growth rates (s^{-1}) of unstable modes 2, 3, and 4 as a function of α . (b) The amplitude of the deviation (m) of the potential vorticity fronts in the linear model $\eta_{k,j}$ (see the appendix and Fig. 6 for their numbering). (c) Growth rate diagram as a function of the radii ratio between the outer and inner contours ($R - R'/R$), and as a function of the ratio between the first Rossby radius R_1 and the vortex radius R .

poles (Carton and McWilliams 1989; Carton and Legras 1994; Baey and Carton 2002), are stable features of the vortex family in a five-layer shallow-water model. The weak instability does not break the initial circular core of the vortex into smaller vortices. Instead, the potential vorticity rearranges the flow into apparently more stable, axisymmetric, multipolar structures.

4. Interaction of a shielded vortex with β effect and topography

The area of formation of the Loop Current rings in the eastern Gulf of Mexico is rich in topographic features that can potentially influence the stability and the propagation properties of oceanic vortices. Three prominent topographic features are worth noting in this area: the Campeche Bank south-southwest of the Loop Current northward extension, the continental southward slope in the northern part of the Gulf, and the western Florida shelf east of the Loop Current (Fig. 9). The Loop Current ring is trapped among these three topographic features during its formation and until long after its separation from the Loop Current. Adding the planetary vorticity gradient on top of the topographic features increases the constraints on the behavior of the Loop Current and the Loop Current ring (Hurlburt and Thompson 1982). Because of differences in shape and position, each of the above-mentioned features has a different influence on the Loop Current. Therefore, sections 4a and 4b are, respectively, dedicated to the study of the individual effect on the pentapole of the planetary vorticity and of the Campeche Bank, taken here as a submarine cape. In section 4c we study the combined effect of the Campeche “cape” and the northern southward slope. In section 4d the presence of the northern shelf of the Campeche Bank (west of the cape) and the western Florida shelf are taken into account.

a. Influence of the β effect on a shielded vortex

Section 3 demonstrated that the vortex instability of a Loop Current-like ring yields the formation of a pentapole on an f plane. On a β plane, however, the stability problem cannot be as clearly posed, since the initial vortex is no longer a steady solution. The β effect combines with the propagation dynamics, which contribute to axial asymmetry. As shown by Dewar and Killworth (1995) and Morel and McWilliams (1997), there is a tendency for the development of a mode 1 perturbation to be induced by the β effect. The influence of β can be strong enough so that the end product of the instability can be quite different from that on the f plane.

Figure 10 presents the nonlinear states, on a β plane,

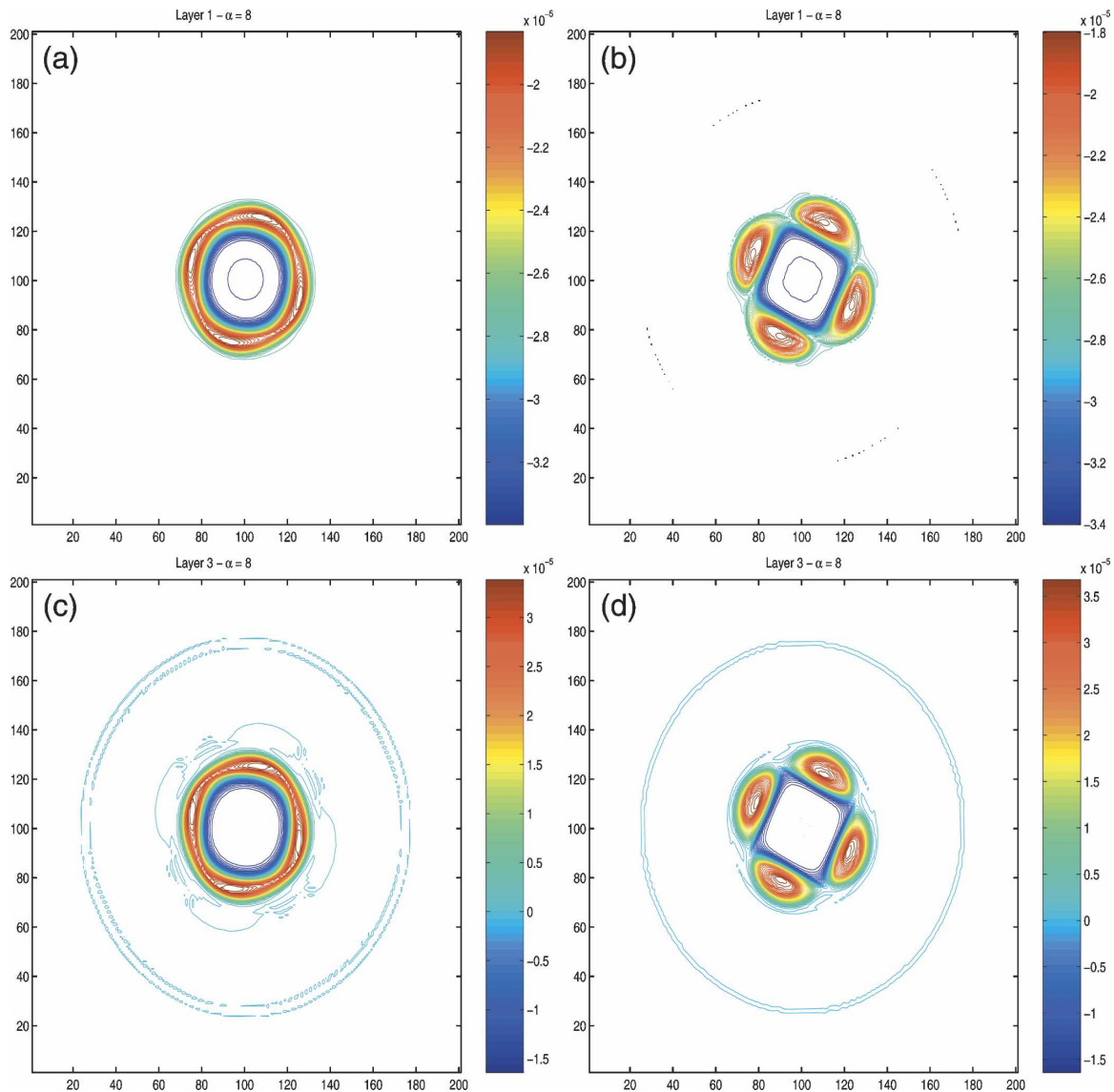


FIG. 8. PVA (s^{-1}) contours of the idealized model of the Loop Current ring showing the formation of a stable pentapole on an f plane in layer 1 on (a) day 25 and (b) day 50. (c), (d) As in (a), (b) but for layer 3.

of the same eddy described in section 3b for the f plane (Fig. 8, $\alpha = 8$). The β effect causes the development of a secondary cyclonic circulation, north of the anticyclone, as the result of the mode 1 perturbation on the initial shielded vortex. Dewar and Killworth (1995) showed a similar behavior in their study of oceanic ring stability based on the influence of deep corotating and counterrotating currents. Their study showed that oceanic eddies with counterrotating deep flows are more unstable than those with corotating deep flows and therefore more sensitive to the β effect. The end product of their nonlinear instability on a β plane (most unstable mode $m = 2$) was also the formation of a

cyclonic circulation north of the initial vortex. In our simulation, the nonlinear state changes from a horizontal dipole to a more turbulent state in which the anticyclone is split by cyclones as the whole system moves to the west as a result of the β effect. As a result of the interaction between mode 1 (forced by β) and mode 4, the most unstable mode is changed to mode 3. The perturbation grows on the rim of the shielded vortex with a strong asymmetry in the cyclones' strength, and the splitting and filamentation are enhanced. The higher-mode instability interaction with the β effect breaks the coherence of a vortex with corotating deep flows.

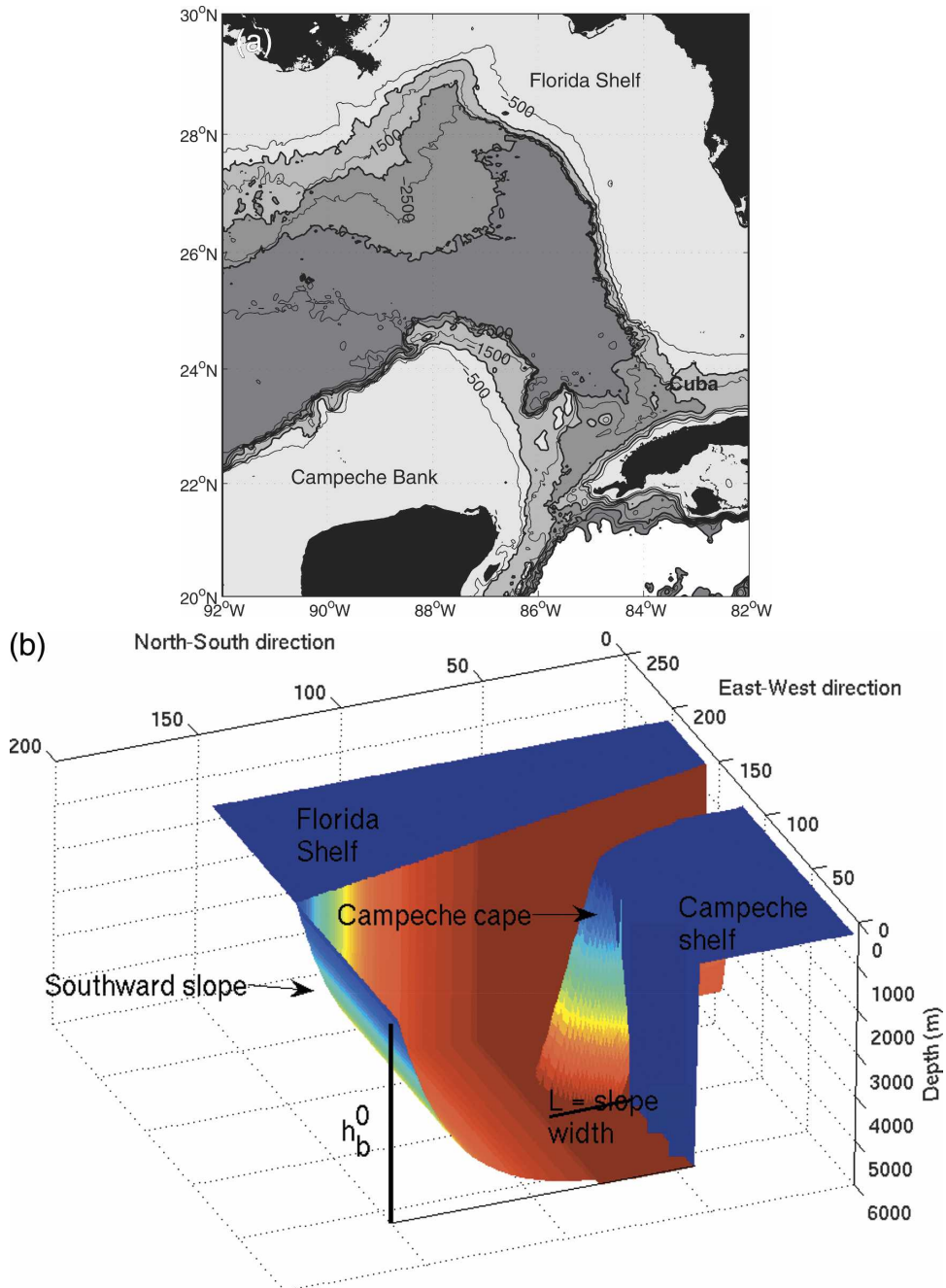


FIG. 9. Bottom topography of the Gulf of Mexico: (a) real topography (m) and (b) idealized topography with an exponentially decaying southward slope as used in the nonlinear experiments. Here, L is the width of the slope of the Campeche Cape and h_b^0 is the height of the northern southward slope. Both are varied individually in the numerical experiments. Each feature of the topography could be removed by choice according to the purpose of the study.

b. Influence of the Campeche Bank on a shielded vortex on an f plane

In the southern Gulf of Mexico, the Campeche Bank extends, at depths between 200 and 500 m, for 280 km

northward of the Yucatan Peninsula coast (Fig. 9). The underwater northern tip of the Campeche Bank is relatively sharp and drops within 50–100 km to 3000-m depth. The shape and slope of the Campeche shelf act as a subsurface cape on the Loop Current ring as it

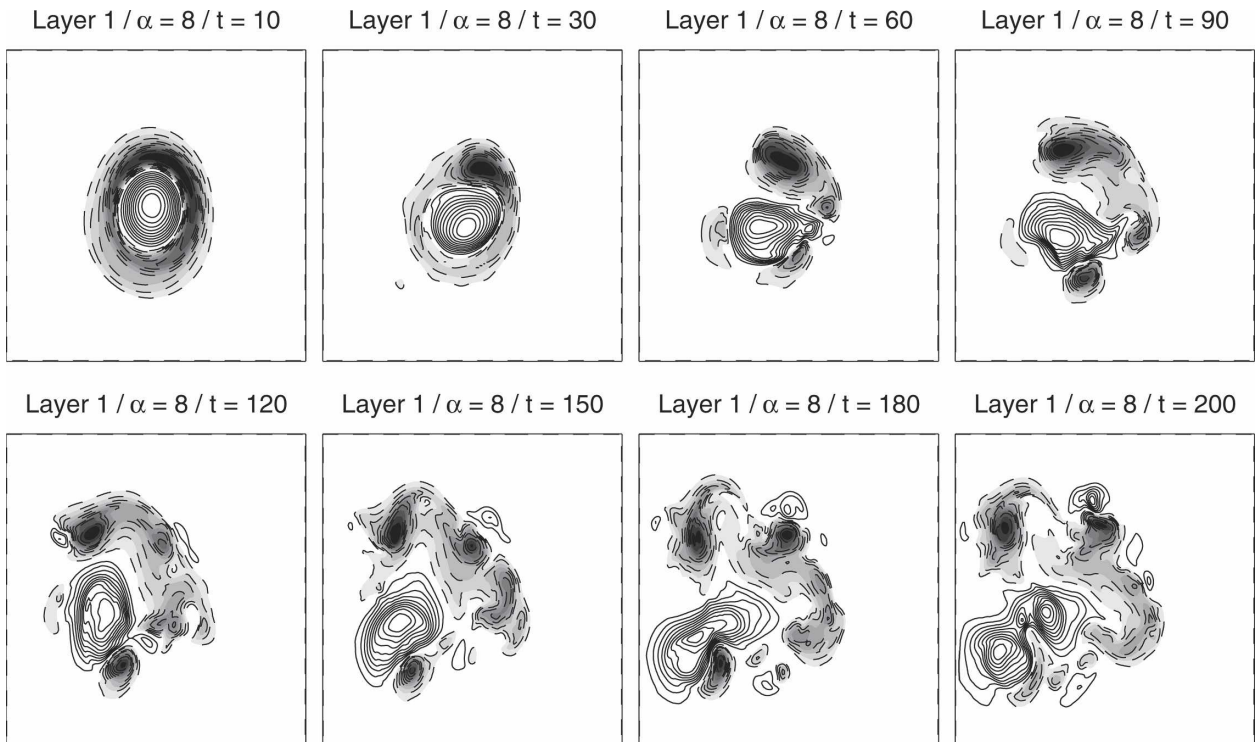


FIG. 10. Layer 1 thickness anomaly (m) contours showing the nonlinear time (t) evolution of the shielded vortex on a β plane. Solid line contours correspond to positive thickness anomalies and dashed and shaded contours correspond to negative thickness anomalies.

grows in the basinlike area defined by the northeast shelf of the Campeche Bank, the north coast of Cuba, and the western Florida shelf.

To estimate the influence of the Campeche Bank shape on the Loop Current rings, the bank is modeled as either a circular or an elliptic subsurface cape with a linear sloping shelf. The influence of the shelf slope and the relative position of the subsurface cape to the Loop Current ring are better studied on an f plane with the center of the vortex positioned north of the cape. If the subsurface cape is wide enough, as a finite-amplitude perturbation of mode-1 type, the subsurface cape perturbation interacts with the mode-4 ring perturbation, yielding a mode-3 perturbation growing on the ring (Fig. 11). For narrow subsurface capes (not illustrated), higher-mode perturbations are forced and smaller-scale cyclones and filaments are generated. The difference in shape of the subsurface cape induces a difference in the erosion of the vortex on the slope via filamentation. The erosion of the vortex will also depend on its proximity to the subsurface cape (Herbette et al. 2003). Sharp subsurface capes (i.e., elliptic) produce less filamentation of the vortex core than wide subsurface capes (i.e., circular). In both the elliptic and circular cases, the subsurface cape introduces an asymmetry into the distribution of the cyclones, with the strength

of the cyclones increasing with the slope of the shelf as shown in Fig. 11. Advection of water by the vortex off the slope, on the western side of the vortex, generates cyclonic vorticity by conservation of potential vorticity. The sizes of these anomalies depend on the magnitude of the shelf slope. They are larger for steep slopes and they increase vortex splitting.

c. Influence of the southward slope in the presence of Campeche Cape

In this section, we investigate the influence of the continental southward-sloping bottom located north of the Loop Current ring in the Gulf of Mexico. The Campeche Cape is also present in the simulation but only the effects of the continental southward slope are discussed. The results are analyzed in terms of cyclone population around the anticyclonic core, as this is the main product of the instability and topography interaction process. Figure 12 shows the differences in cyclone population and intensity in layer 3 for several configurations. In this study, the steepness of the southward continental slope is defined by the height of the slope at the coast, h_b^0 .

Jacob et al. (2002) showed that a considerable reduction in the eddy propagation speed can be induced by a southward linear slope that opposes the β effect in the

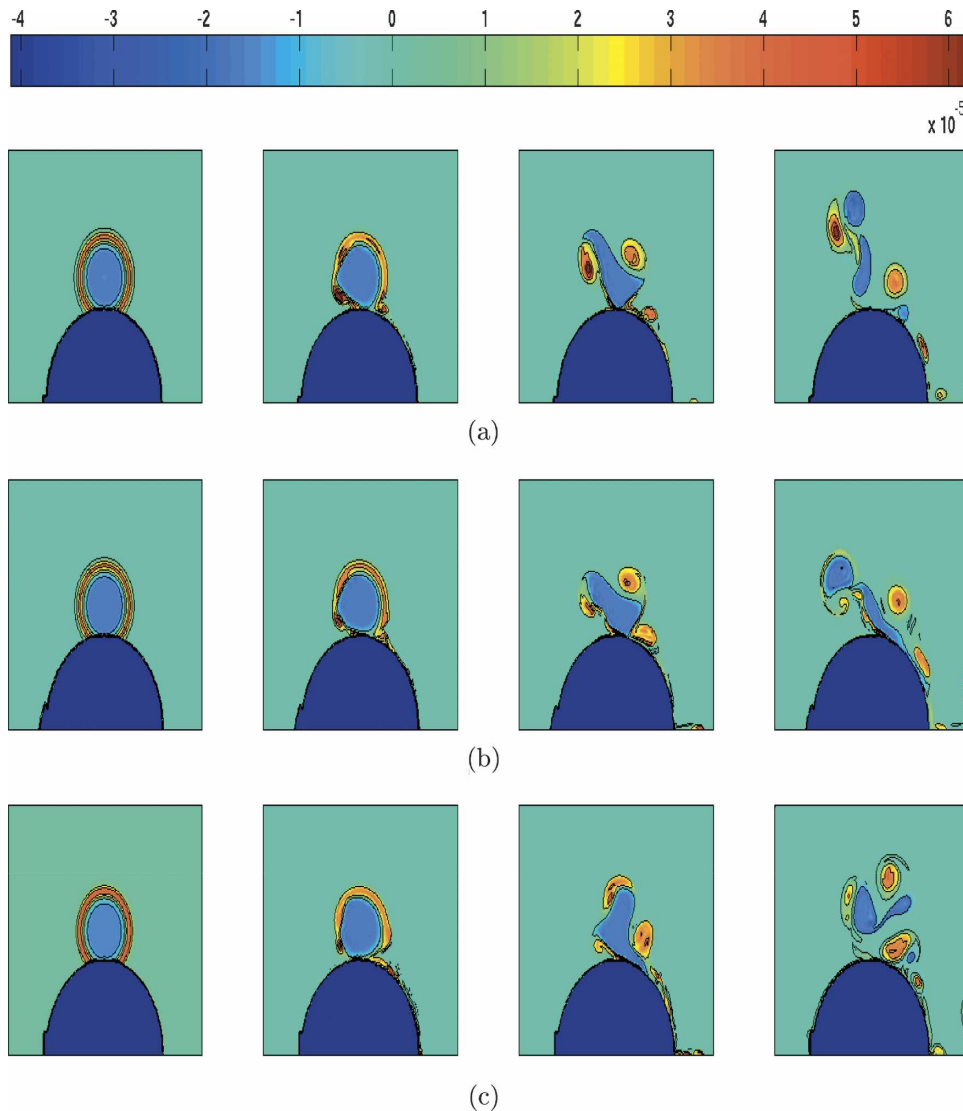


FIG. 11. Time evolution of the potential vorticity anomaly (s^{-1}) in layer 3 of the Loop Current ring numerical model for days 1, 10, 30, and 60 (from left to right). The effects of increasing the slope width L (Fig. 9) of the circular Campeche Bank on the ring: (a) vertical wall, (b) 100 km wide, and (c) 200 km wide. Dark blue indicates the topography. As in reality, the top of the shelf is at 200 m below the surface.

bottom layer. Moreover, the decay of the eddy was found by Jacob et al. (2002) to be much slower than in the case with only the β effect, and the eddy retained its strength over a longer period of time. For the idealized Loop Current ring case and in the absence of β , the ring ends up drifting to the east on the southward slope as shown in Fig. 12a. The erosion of the vortex by filamentation is therefore reduced since it moves away from the Campeche Bank (elliptic shape acts to minimize the erosion of the vortex on the slope).

The competition between β and the steepness of the slope is illustrated in Figs. 12b and 12c. In the case of the steepest linear slope experiment (Fig. 12b), the an-

ticyclonic ring is more strongly sheared by the cyclone population when compared with an experiment with a slope not as steep (Fig. 12c). With the decrease in slope steepness, filamentation of the deep anticyclone is as strong and the cyclone interaction with the anticyclone is less effective than in the steep slope case. The shape of the slope also matters: the influence of the cyclones was found to be smaller with an exponentially varying slope (Fig. 12d) than with a linear southward slope experiment, in general, since the cyclones are farther away from the anticyclone. The dispersion of the cyclonic belt by topographic Rossby waves is found to be weaker in the absence of β (Fig. 12a). Furthermore, the

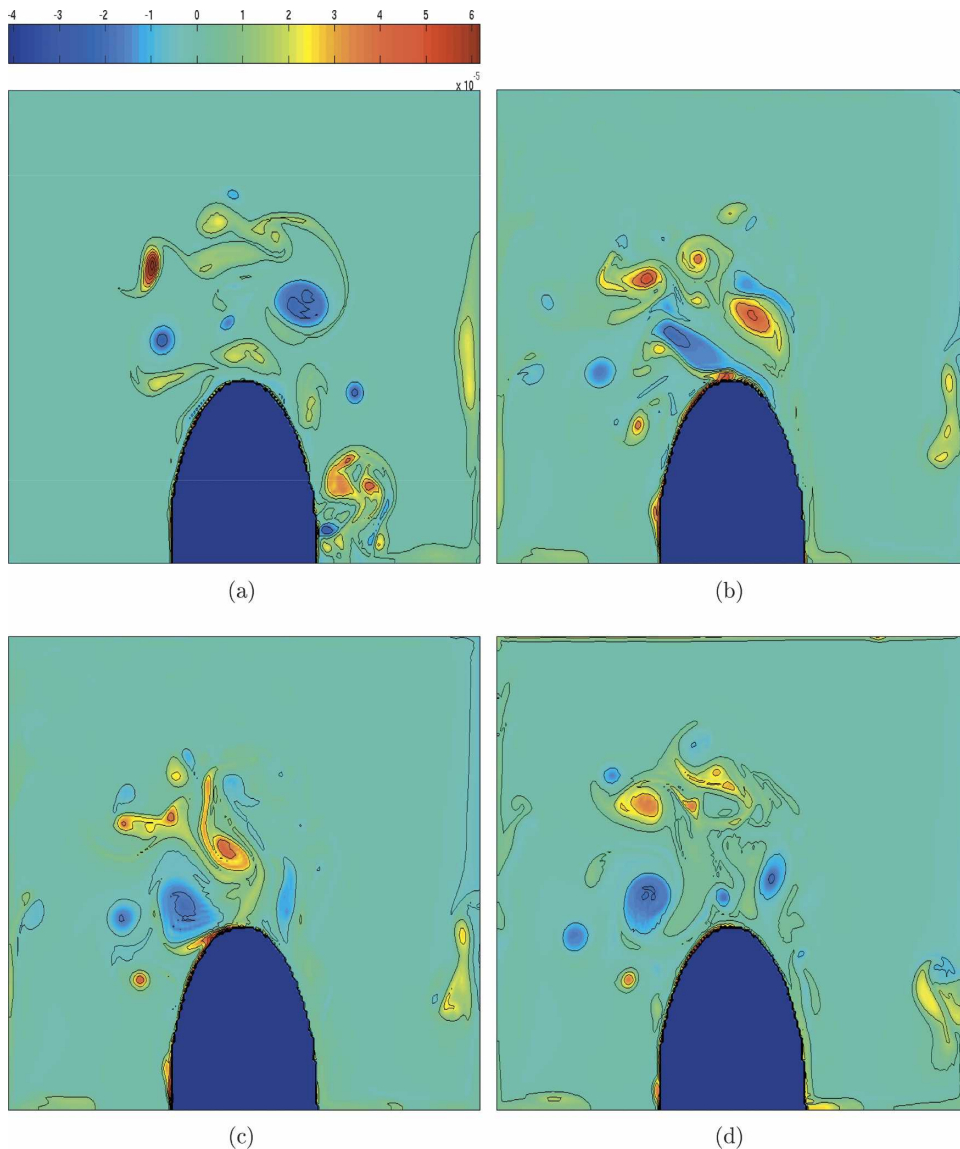


FIG. 12. Potential vorticity anomaly (s^{-1}) in Loop Current ring model layer 3, at day 130, for various southward continental bottom slopes [blue (red) contours show anticyclones (cyclones), and dark blue indicates the topography]: (a) with no β effect, with $h_b^0 = 3030$ m, and a linear bottom slope, and (b) same as in (a) but with the β effect; (c) with the β effect and $h_b^0 = 2500$ m, and a linear bottom slope, and (d) same as in (c) but with $h_b^0 = 4650$ m and an exponential bottom slope.

anticyclonic core is found to remain coherent, in contrast with the findings of Thierry and Morel (1999), who showed that large rings (radius > 100 km) become unstable on very steep slopes and are dispersed by topographic Rossby waves.

We now look at the surface signature of the anticyclone (Fig. 13). Thierry and Morel (1999) and Jacob et al. (2002) found that steep slopes increase deep eddy flow scattering by topographic Rossby waves and weaken the deep parts of vortices, increasing their sensitivity to filamentation and splitting. The anticyclone is

indeed found to interact more with the surrounding cyclones (Fig. 13a) as it is weakened by the steep southward linear topography. When scattering is not as strong in the lower layer, the anticyclone is more coherent than when the southward slope is steep (high scatter) and the anticyclone–cyclone interaction is not as strong (Fig. 13b). In the presence of an exponentially sloping bottom (Fig. 13c), the bottom slope effect changes meridionally. Cyclones, north of the anticyclone, are more dispersed than the anticyclone. The anticyclone retains its strength longer, while the cy-



FIG. 13. (a) The layer 1 thickness anomaly at day 130 for various continental southward bottom slopes with the β effect and $h_b^0 = 3030$ m. (b) Same as in (a) but with $h_b^0 = 2500$ m. Positive (negative) values are contoured (shaded and dashed lines). (c) The southward exponential bottom slope with $h_b^0 = 4650$ m.

clones quickly weaken. Therefore, the interaction of the anticyclone with the cyclone is also reduced. With no southward slope and with β , the anticyclone–cyclone interaction is strong, and the anticyclone is eroded and split by the cyclone and by the Campeche Bank in the deep layers. Only the cyclone keeps its initial strength (not shown).

In summary, the upper-layer anticyclone behaves like the lower one in terms of its interaction with the cyclone and production of filaments. It is worth noting that the filaments are produced in the deep layers (below 300 m), where the vortex core leans on the Campeche Bank slope. Vortex stretching induces filament signatures in the surface layer (Fig. 13), but the vortex width remains larger than in the deep layers.

d. Ring propagation speed

Various westward propagation speeds are obtained for the idealized configurations described so far. The observations suggest that the westward zonal drift should be between 2 and 5 km day⁻¹ (Coats 1992; Elliott 1982; Shay et al. 1998; Schmitz 2003). The Loop Current ring drift in the high-resolution MICOM simulation, with values on the order of 4 km day⁻¹, shows good agreement with the observations. However, the idealized Loop Current rings in the above experiments do not move as fast, thus suggesting that the β effect alone may not be sufficient to account for the westward drift of Loop Current rings as has been surmised (Hurlburt and Thompson 1982). The importance of the continental southward slope on the westward drift is illustrated in Fig. 14 for experiments where the Campeche Bank is represented as one-half of an ellipse pointing to the north and where the vortex is initialized north of the tip of the cape.

With no β effect and $h_b^0 = 3030$ m, the displacement of the anticyclone is actually to the east (Fig. 14a). With the β effect and the same slope, the eddy drift remains small since the bottom slope mostly cancels the β effect in the bottom layer. The westward drift increases as the bottom slope is decreased ($h_b^0 = 2500$ m), but the eddy is still in contact with the Campeche Cape after 150 days. With an exponential slope, the zonal drift is increased: the ring core is ≈ 400 km away from its initial position after 150 days, instead of 250 km away with a linear slope.

When the northern shelf of the Campeche Bank (same slope and height as the cape) is added to the west of the cape, the westward propagation speed is significantly increased, and realistic propagation speeds, corresponding to the average speed found in observations and in realistic numerical models, are obtained. Moreover, the deep anticyclone separates completely from

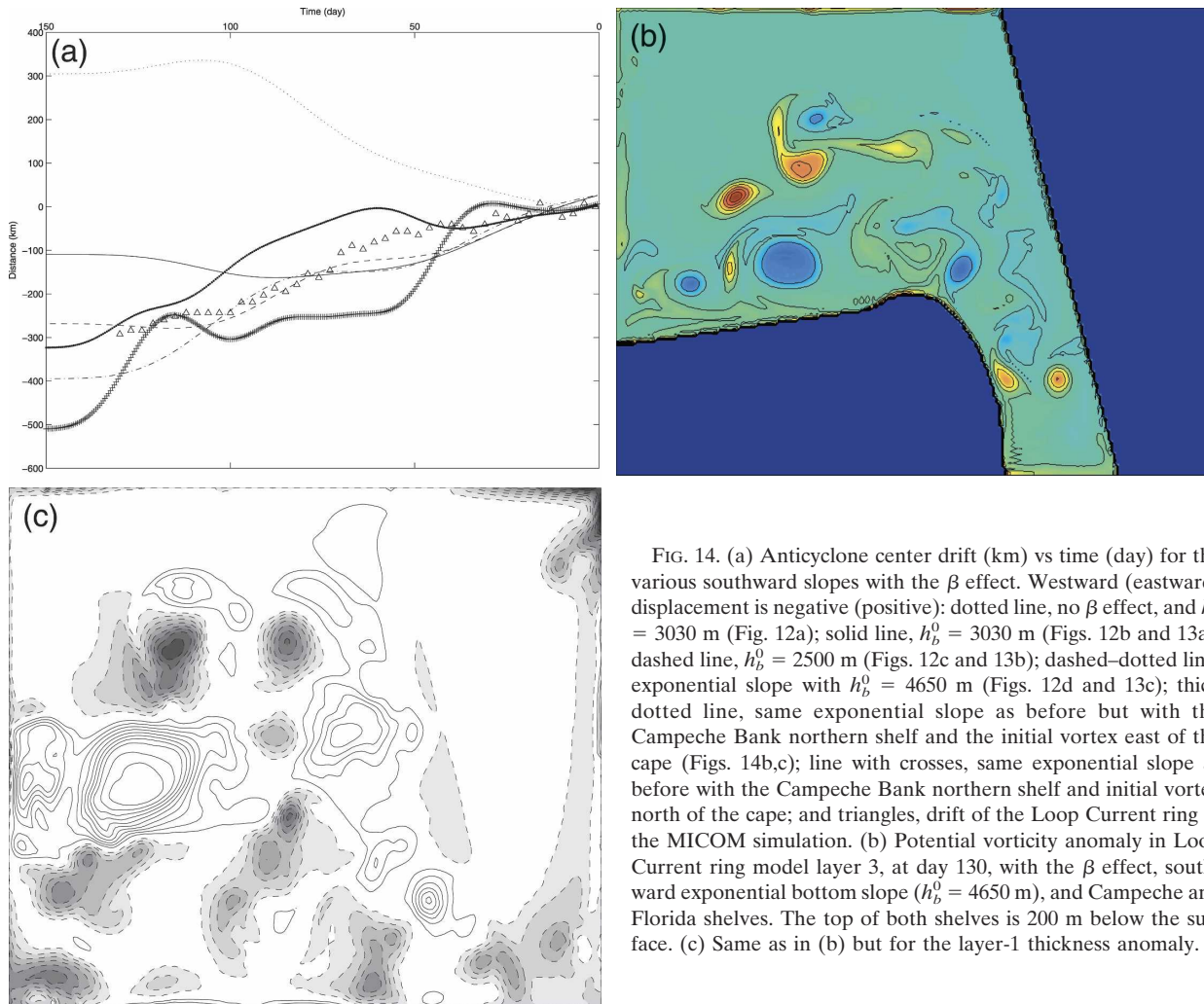


FIG. 14. (a) Anticyclone center drift (km) vs time (day) for the various southward slopes with the β effect. Westward (eastward) displacement is negative (positive): dotted line, no β effect, and $h_b^0 = 3030$ m (Fig. 12a); solid line, $h_b^0 = 3030$ m (Figs. 12b and 13a); dashed line, $h_b^0 = 2500$ m (Figs. 12c and 13b); dashed-dotted line, exponential slope with $h_b^0 = 4650$ m (Figs. 12d and 13c); thick dotted line, same exponential slope as before but with the Campeche Bank northern shelf and the initial vortex east of the cape (Figs. 14b,c); line with crosses, same exponential slope as before with the Campeche Bank northern shelf and initial vortex north of the cape; and triangles, drift of the Loop Current ring in the MICOM simulation. (b) Potential vorticity anomaly in Loop Current ring model layer 3, at day 130, with the β effect, southward exponential bottom slope ($h_b^0 = 4650$ m), and Campeche and Florida shelves. The top of both shelves is 200 m below the surface. (c) Same as in (b) but for the layer-1 thickness anomaly.

the cape and drifts westward along the Campeche shelf (Figs. 14b and 14c). This increase in the translation speed can be explained by the mirror effect of the coast on the vortex. The northern topography of the Campeche Bank acts as a waveguide that increases the anticyclone advection to the west. Without the Campeche shelf, when the vortex is initialized east of the cape, the motion to the west is blocked and erosion on the Campeche Cape creates filaments and splitting of the anticyclone. The presence of the northern Campeche shelf west of the cape contributes to the passage of the ring west of the cape (Fig. 14a, thick dotted line). As in the realistic MICOM simulation (Fig. 14a, triangles), the propagation speed is slow in the vicinity of the cape and increases toward the west of the cape.

The addition of the Florida shelf actually reduces significantly the drift of the vortex for both types of continental slopes, but much less so for a linear slope

than for an exponential one. As the distance d between the Campeche Bank eastern shelf and the Florida shelf decreases, trapping of the anticyclone–cyclone dipole increases. To maintain a reduced influence of the Florida western shelf, a distance $d > R$ is necessary, where R is the radius of the outer rim of the cyclonic belt.

It is worth noting that in all the experiments described above, more than one cyclone is observed north of the anticyclone. In all cases, however, there is always one cyclone that also drifts westward north of the anticyclone, forming a horizontal dipole with the anticyclone both in the deep and surface layers (Figs. 12 and 13), as observed in other numerical simulations (Sturges et al. 1993; Oey 1996; Murphy et al. 1999; Chérubin et al. 2005). However, in the models of Sturges et al. (1993) and Welsh and Inoue (2000), the dipole is not oriented north–south and does not appear in the surface layers.

5. Summary and conclusions

Observations based on satellite SSH maps and numerical modeling show the presence of cyclones in the vicinity of the Loop Current ring, from before its separation from the Loop Current until its decay in the western Gulf. In this study, we have focused on the origin of the cyclones in the vicinity of the Loop Current ring before the separation from the Loop Current itself. Using the ECMWF daily forced high-resolution MICOM simulation for the North Atlantic as a benchmark experiment, we confirmed that the separation of the Loop Current ring and the generation of cyclones in its vicinity were the consequence of an instability (Chérubin et al. 2005). The present study shows that the instability is mixed: barotropic instability is surface intensified while baroclinic instability is bottom intensified. Each of the shedding events in the MICOM simulation is associated with an increase of the potential vorticity anomaly gradient across the vortex. The core becomes more negative, while on the rim of the vortex, a positive anomaly grows. This particular feature allows us to classify this vortex as a shielded or “R” vortex (Flierl 1988; Morel and McWilliams 1997), the instability properties of which are known: higher unstable modes grow as the width of the shield decreases. The linear instability study showed that mode 4 is the most unstable mode of a Loop Current ring-like vortex and the nonlinear regime evolved in a steady pentapole on an f plane.

We then investigated the interaction of the Loop Current-like vortex with the β effect, which transforms the vortex into an unstable quadrupole as the result of the interaction between modes 4 and 1, the latter being forced by the planetary vorticity gradient. The cyclonic ring of the vortex is separated from the anticyclone and both propagate westward as a dipole, the cyclone being north of the anticyclone.

When a topographic feature equivalent to the submarine promontory of the Campeche Bank, south-southwest of the Loop Current ring, is added, filamentation and vortex splitting are enhanced by the submarine cape. Filamentation increases with the width and slope of the cape. The cape acts as a finite-amplitude perturbation, which interacts with the most unstable mode of the vortex. The generation of cyclones varies with the size of the cape. Besides the cape effect, because of the β effect the main cyclone is formed north of the anticyclone. The strength of the cyclone contributes to the anticyclone splitting.

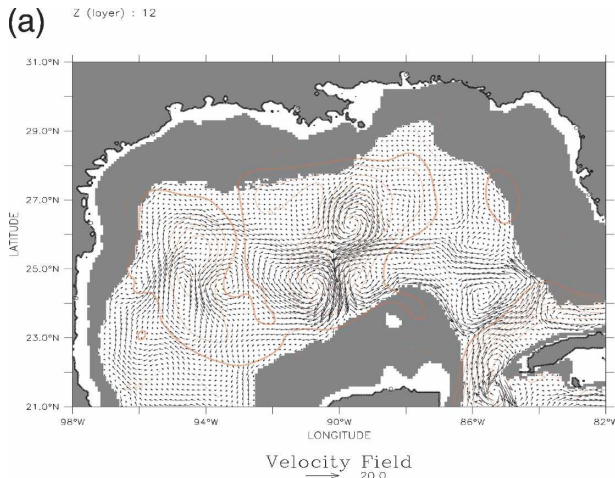
In the presence of a southward slope north of the vortex, scattering of the northern cyclone and of the anticyclone is increased in the deep layer. It has a vis-

ible signature at the surface, and the steepness of the slope controls the westward propagation speed of the anticyclone. Since the cyclone is north of the anticyclone, the strength of the cyclone is decreased by scattering, more so than is the strength of the anticyclone. The latter remains coherent and propagates faster to the west. Changing the slope profile, from linear to exponential, increases the northern cyclone scattering by topographic Rossby waves. The anticyclone interacts less with the cyclones and travels faster to the west. This result reveals the crucial role of the southward slope north of the Loop Current.

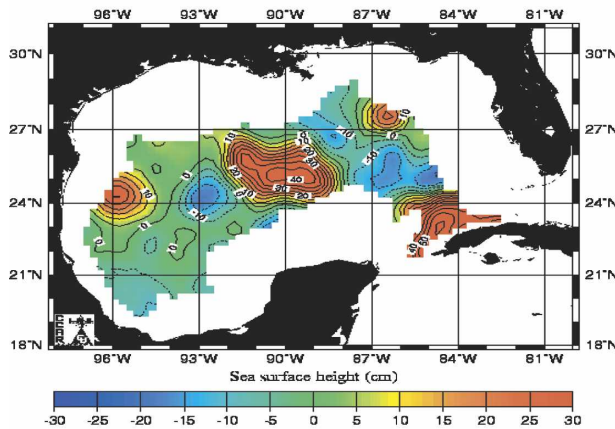
The presence of the northern shelf of the Campeche Bank increases the westward propagation of the anticyclone by adding the velocity component of its mirror effect of the coast and by adding the fast-velocity component of the westward propagation of topographic Rossby waves. This shelf was also shown to favor the crossing of the cape by the anticyclone when its initial location was east of the cape. The northern Campeche shelf also compensates for the blocking effect of the western Florida shelf.

The MICOM simulation indeed confirms that the anticyclone follows the 1000-m depth contour of the Campeche shelf until it interacts with the western Gulf circulation (Fig. 15a). This result is indeed obtained in most Gulf of Mexico numerical simulations (Hurlburt and Thompson 1980; Sturges et al. 1993; Oey 1996; Murphy et al. 1999; Welsh and Inoue 2000), but was never previously noticed. SSH maps from the Real-Time Altimetry project at the Colorado Center for Astro-dynamics Research show the Loop Current ring following the 1500-m contour isobath (Figs. 15b and 15c). The propagation speeds in the idealized numerical model and in the MICOM simulation are in the range of the observed speeds (2–5 km day⁻¹), with an average (observed) of 4 km day⁻¹. The MICOM simulation also shows the pervasive role and presence of cyclones both at the surface and in the deep layers. In addition to the northern cyclone that forms, with the anticyclone, a feature that was called a modon in previous model results (Sturges et al. 1993; Oey 1996; Murphy et al. 1999; Welsh and Inoue 2000), more cyclones surround the anticyclone during its formation and its propagation to the west, especially in the deep layers as observed in the idealized model.

In summary, this study shows the generation of cyclones by the Loop Current ring instability before separation. The cyclones are therefore generated at the same instant at three different locations, rather than one at a time at a single location. The growth of cyclones between the Loop Current and the ring most



(b) Historical Mesoscale Altimetry - Jun 15, 1998



(c) Historical Mesoscale Altimetry - Jul 15, 1998

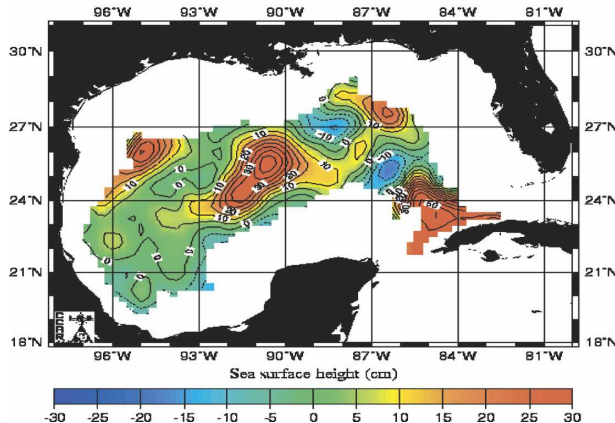


FIG. 15. Snapshots showing (a) the Loop Current ring following the Campeche shelf during its westward propagation in the MICOM simulation [red SSH (cm) contours superimposed on velocity vectors in layer 12 (≈ 1000 m deep)] and (b) in SSH map above waters deeper than 1500 m from the Real-time Altimetry project of Colorado Center for Astroynamics Research on 15 Jun 1998. (c) Same as in (b) but on 15 Jul 1998.

likely contributes to their separation at the surface as in the deep layers, as shown by the MICOM simulation.

Acknowledgments. The study is supported by the Mineral Management Service under Contracts 1435-01-00-CT-31076 and 01-99-CT-31028 (via SAIC) and by NSF Grant OCE 03-271808. The authors thank Professors X. J. Carton, W. J. Schmitz Jr., and W. Sturges for fruitful discussions and contributions to this paper. They also thank L. T. Smith for careful reading and editing of the manuscript.

APPENDIX

Linear Instability Calculations

The derivation of the analytical model is given in cylindrical coordinates. The perturbation (or Rayleigh) equations are derived at the PVA front in each layer starting from the relation between streamfunction and PVA in the QG formalism. The PVA is related to the streamfunction through the general equation

$$\mathbf{PVA} = \nabla^2 \Psi + \mathbf{Fr} \Psi, \quad (\text{A1})$$

where $\mathbf{PVA} = [\text{PVA}_1, \dots, \text{PVA}_k, \dots, \text{PVA}_N]$, $\Psi = [\psi_1, \dots, \psi_N]$, and \mathbf{Fr} is an $N \times N$ matrix that is associated with the stretching term. As potential vorticity is assumed piecewise constant, we can thus write

$$\text{PVA}_k = \sum_j \Delta_{k,j} \mathcal{H}(r_{k,j} + \eta_{k,j} - r), \quad (\text{A2})$$

where \mathcal{H} is the Heaviside function, $\Delta_{k,j} = Q_{k,j} - Q_{k,j+1}$ is the potential vorticity jump at the j th contour $r = r_{k,j} + \eta_{k,j}(\theta, t)$ in the k th layer, $r_{k,j}$ is the initial radius, and $\eta_{k,j}$ is its deformation. As gradients of Q_k give delta functions, Lagrangian conservation of PVA_k yields

$$\begin{aligned} \frac{D}{Dt} \text{PVA}_k &= \sum_j -\Delta_{k,j} \delta(r_{k,j} + \eta_{k,j} - r) \left(\frac{D}{Dt} r \right. \\ &\quad \left. - \frac{D}{Dt} \eta_{k,j} \right) \\ &= 0, \quad k = 1, \dots, N. \end{aligned} \quad (\text{A3})$$

Assuming small perturbations of the initial potential vorticity fronts, we can decompose the initial axisymmetric flows as $\psi_{k,j} = \bar{\phi}_k(r) + \phi'_k(r, \theta, t)$, where ϕ'_k is associated with the perturbation. The initial part of the axisymmetric flows $\bar{\phi}_k$ satisfies for each layer k

$$\begin{aligned} \nabla^2 \bar{\phi}_k + \mathbf{Fr} \bar{\phi}_k &= \frac{d^2 \bar{\phi}_k}{dy^2} + \mathbf{Fr} \bar{\phi}_k = \sum_j \Delta_{k,j} \mathcal{H}(r_{k,j} - r), \\ k &= 1, \dots, N, \end{aligned} \quad (\text{A4})$$

from which we derive the angular velocity

$$\bar{\Omega}_k = \frac{1}{r} \frac{d\bar{\phi}_k}{dr}.$$

Linearization of Eq. (A3) gives the Rayleigh equation

$$\frac{\partial}{\partial t} \eta_{k,j} + \bar{\Omega}_k \frac{\partial}{\partial \theta} \eta_{k,j} = -\frac{1}{r_{k,j}} \frac{\partial}{\partial \theta} \phi'_{k,j}. \quad (\text{A5})$$

Writing $\eta_{k,j} = \eta_{k,j} \exp[i l(\theta - ct)]$ and $\phi'_k = \phi'_k(y) \exp[i l(\theta - ct)]$, ϕ'_k then satisfies the equation

$$\nabla^2 \phi'_k + \mathbf{Fr} \Phi'_k |_{k} = \sum_j \Delta_{k,j} [\mathcal{H}(r_{k,j} + \eta_{k,j} - r) - \mathcal{H}(r_{k,j} - r)], \quad (\text{A6})$$

$$k = 1, \dots, N,$$

which gives at leading order in the small η limit

$$\nabla^2 \phi'_k + (\mathbf{Fr} - l^2) \Phi'_k |_{k} = \sum_j \Delta_{k,j} \eta_{k,j} \delta(r - r_{k,j}). \quad (\text{A7})$$

The last step is to solve Eqs. (A3), (A4), and (A7) for azimuthal mode l . Equations (9) and (11) are similar and their general form can be written

$$\nabla_l^2 \phi_k + \mathbf{Fr} \Phi_k |_{k} = \Gamma_k, \quad (\text{A8})$$

with

$$\nabla_l^2 = \frac{1}{r} \frac{\partial}{\partial r} r \frac{\partial}{\partial r} - \frac{l^2}{r^2}$$

and Γ_k , the PV jumps at the PV fronts. This equation can be solved in terms of vertical modes $\mathbf{P}^{(n)} = [P_1^{(n)}, \dots, P_k^{(n)}, \dots, P_N^{(n)}]$ associated with the vortex-stretching matrix \mathbf{Fr} , so that

$$\mathbf{Fr} \mathbf{P} = -\mathbf{D} \mathbf{P}, \quad (\text{A9})$$

where $\mathbf{P} = [\mathbf{P}^{(1)}, \dots, \mathbf{P}^{(N)}]$ is the eigenvector matrix and $\mathbf{D} = [\gamma_n^2]$ is the diagonal matrix mode of the eigenvalues. Here, $R = \gamma_n^{-1}$ is the radius of deformation associated with the n th mode.

We also define a matrix $\boldsymbol{\lambda}$, with coefficients $\lambda_k^{(n)}$, so that $\boldsymbol{\lambda}$ is the inverse of the eigenvector matrix $\mathbf{P}[\sum_k \lambda_k^{(m)} P_k^{(n)} = \delta_{nm}]$. Thus, if we set

$$\phi_k = \sum_n \phi^{(n)} P_k^{(n)} \quad \text{and} \quad \Gamma_k = \sum_n P_k^{(n)} \Gamma^{(n)},$$

then

$$\Gamma^{(n)} = \sum_l \alpha_l^{(n)} \Gamma_l,$$

and $\phi^{(n)}$ satisfies

$$\nabla_l^2 \phi^{(n)} - \gamma_n^2 \phi^{(n)} = \Gamma^{(n)}. \quad (\text{A10})$$

The solution of this equation is obtained from Green's function for the Helmholtz operator of the left-hand side (see Abramovitz and Stegun 1972) when $\Gamma^{(n)} = \delta(r' - r)$. The details of the calculations are given by Vandermeersch et al. (2001). Thus, we obtain the analytical form of the perturbed streamfunction that we use along with the initial axisymmetric flow $\bar{\Omega}_k$, in Eq. (A5), which is solved in the normal mode framework. The growth rates of the unstable wavenumber l are the eigenvalues of the system.

REFERENCES

- Abramovitz, M., and I. Stegun, 1972: *Handbook of Mathematical Functions*. Dover, 1046 pp.
- Baey, J.-M., and X. Carton, 2002: Vortex multipoles in two-layer rotating shallow-water flows. *J. Fluid Mech.*, **460**, 151–175.
- Biggs, D. C., G. S. Fargion, P. Hamilton, and R. R. Leben, 1996: Cleavage of a Gulf of Mexico loop current eddy by a deep water cyclone. *J. Geophys. Res.*, **101**, 20 629–20 641.
- Bleck, R., 1985: On the conversion between mean and eddy components of potential and kinetic energy in isentropic and isopycnic coordinates. *Dyn. Atmos. Oceans*, **9**, 17–37.
- Boss, E., N. Paldor, and L. Thomson, 1996: Stability of a potential vorticity front: From quasi-geostrophy to shallow-water. *J. Fluid Mech.*, **315**, 65–84.
- Candela, J., J. Sheinbaum, J. L. Ochoa, A. Badan, and R. Leben, 2002: The potential vorticity flux through the Yucatan Channel and the Loop Current in the Gulf of Mexico. *Geophys. Res. Lett.*, **29**, 2059, doi:10.1029/2002GL015587.
- Carton, X. J., and J. C. McWilliams, 1989: Barotropic and baroclinic instabilities of axisymmetric vortices in a QG model. *Mesoscale/Synoptic Coherent Structures in Geophysical Turbulence*, J. C. J. Nihoul and B. M. Jamart, Eds., Elsevier Oceanographic Series, Vol. 50, Elsevier, 225–244.
- , and B. Legras, 1994: The life-cycle of tripoles in 2D incompressible flows. *J. Fluid Mech.*, **267**, 53–82.
- Charney, J. G., and M. E. Stern, 1962: On the instability of internal baroclinic jets in a rotating atmosphere. *J. Atmos. Sci.*, **19**, 159–172.
- Chassignet, E. P., and D. B. Boudra, 1988: Dynamics of Agulhas retroreflection and ring formation in numerical model. Part II. Energetics and ring formation. *J. Phys. Oceanogr.*, **18**, 304–319.
- , and Z. D. Garraffo, 2001: Viscosity parameterization and the Gulf Stream separation. *From Stirring to Mixing in a Stratified Ocean: Proc. 'Aha Huliko'a Hawaiian Winter Workshop*, Honolulu, HI, University of Hawaii at Manoa, 37–41.
- , L. T. Smith, R. Bleck, and F. O. Bryan, 1996: A model comparison: Numerical simulations of the North and equatorial Atlantic oceanic circulation in depth and isopycnic coordinates. *J. Phys. Oceanogr.*, **26**, 1849–1867.
- Chérubin, L. M., W. Sturges, and E. P. Chassignet, 2005: Deep flow variability in the vicinity of the Yucatan Straits from a high-resolution MICOM simulation. *J. Geophys. Res.*, **110**, C04009, doi:10.1029/2004JC002280.
- Coats, D. A., 1992: The Loop Current. *Physical Oceanography of the U.S. Atlantic and Eastern Gulf of Mexico*, J. D. Milliman and E. Imamura, Eds., Atlantic OCS Region, Mineral Management Service, U.S. Dept. of the Interior.

- Cochrane, J. D., 1972: Separation of an anticyclone and subsequent developments in the Loop Current. *Contributions on the Physical Oceanography of the Gulf of Mexico*, L. R. A. Capurro and J. L. Reid, Eds., Gulf Publishing, 91–106.
- Dewar, W. K., and P. D. Killworth, 1995: On the stability of oceanic rings. *J. Phys. Oceanogr.*, **25**, 1467–1487.
- Elliot, B. A., 1979: Anticyclonic rings and the energetics of the circulation of the Gulf of Mexico. Ph.D. dissertation, Texas A&M University, College Station, TX, 188 pp.
- , 1982: Anticyclonic rings in the Gulf of Mexico. *J. Phys. Oceanogr.*, **12**, 1292–1309.
- Ertel, H., 1942: Ein neuer hydrodynamischer Wirbelsatz (A new scalar to characterize hydrodynamic eddies). *Meteor. Z.*, **59**, 271–281.
- Flierl, G. R., 1987: Isolated eddy models in geophysics. *Annu. Rev. Fluid Mech.*, **19**, 493–530.
- , 1988: On the instability of geostrophic vortices. *J. Fluid Mech.*, **197**, 349–388.
- Fratantoni, D. M., T. N. Lee, G. P. Podesta, and F. Muller-Karger, 1998: The influence of the Loop Current perturbations on the formation and evolution of Tortugas eddies in the southern Straits of Florida. *J. Geophys. Res.*, **103**, 24 759–24 779.
- Garraffo, Z. D., A. J. Mariano, A. Griffa, C. Veneziani, and E. P. Chassignet, 2001: Lagrangian data in a high-resolution numerical simulation of the North Atlantic. I: Comparison with in situ drifter data. *J. Mar. Syst.*, **29**, 157–176.
- Herbette, S., Y. Morel, and M. Arhan, 2003: Erosion of a surface vortex by a seamount. *J. Phys. Oceanogr.*, **33**, 1664–1679.
- Hoskins, B. J., M. E. McIntyre, and A. W. Robertson, 1985: On the use and significance of isentropic vorticity maps. *Quart. J. Roy. Meteor. Soc.*, **111**, 877–946.
- Hurlburt, H. E., 1985: Cyclonic eddy generation in the Gulf of Mexico. *Proc. Sixth Annual Gulf of Mexico Information Transfer Meeting*, Gulf of Mexico OCS Regional Office, Minerals Management Service, U.S. Dept. of the Interior, 272–273, 283.
- , 1986: Dynamic transfer of simulated altimeter data into subsurface information by a numerical ocean model. *J. Geophys. Res.*, **91**, 2372–2400.
- , and J. D. Thompson, 1980: A numerical study of Loop Current intrusion and eddy shedding. *J. Phys. Oceanogr.*, **10**, 1611–1651.
- , and —, 1982: The dynamics of the Loop Current and shed eddies in a numerical model of the Gulf of Mexico. *Hydrodynamics of Semi-Enclosed Seas*, J. C. J. Nihoul, Ed., Elsevier, 243–298.
- Ichiye, T., 1962: Circulation and water-mass distribution in the Gulf of Mexico. *Geofis. Int.*, **2**, 47–76.
- Inoue, M., 1998: Modeling deep water in the Gulf of Mexico. *Workshop on Environmental Issues Surrounding Deepwater Oil and Gas Development*, R. S. Carney, Ed., OCS MMS 98-0022, Gulf of Mexico OCS Region, Minerals Management Service, U.S. Dept. of the Interior, New Orleans, LA, 163 pp.
- Jacob, J. P., E. P. Chassignet, and W. K. Dewar, 2002: Influence of topography on the propagation of isolated eddies. *J. Phys. Oceanogr.*, **32**, 2848–2869.
- Levitus, S., 1982: *Climatological Atlas of the World Ocean*. NOAA Prof. Paper 13, 173 pp. and 17 microfiche.
- Morel, Y., and X. J. Carton, 1994: Multipolar vortices in two-dimensional incompressible flows. *J. Fluid Mech.*, **267**, 23–51.
- , and J. McWilliams, 1997: Evolution of isolated interior vortices in the ocean. *J. Phys. Oceanogr.*, **27**, 727–748.
- Murphy, S. J., H. E. Hurlburt, and J. J. O'Brien, 1999: The connectivity of eddy variability in the Caribbean Sea, the Gulf of Mexico, and the Atlantic Ocean. *J. Geophys. Res.*, **104**, 1431–1453.
- Ochoa, J., J. Sheinbaum, A. Badan, J. Candela, and D. Wilson, 2001: Geostrophy via potential vorticity inversion in the Yucatan Channel. *J. Mar. Res.*, **59**, 725–747.
- Oey, L. Y., 1996: Simulation of mesoscale variability in the Gulf of Mexico: Sensitivity studies, comparison with observations, and trapped wave propagation. *J. Phys. Oceanogr.*, **26**, 145–175.
- Paiva, A. M., J. T. Hargrove, E. P. Chassignet, and R. Bleck, 1999: Turbulent behavior of a fine mesh (1/12°) numerical simulation of the North Atlantic. *J. Mar. Syst.*, **21**, 307–320.
- Papadakis, M. P., E. P. Chassignet, and R. W. Hallberg, 2003: Numerical simulations of the Mediterranean Sea outflow: Impact of the entrainment parameterization in an isopycnal coordinate ocean model. *Ocean Modell.*, **5**, 325–356.
- Pedlosky, J., 1987: *Geophysical Fluid Dynamics*. Springer-Verlag, 710 pp.
- Romanou, A., E. P. Chassignet, and W. Sturges, 2004: The Gulf of Mexico circulation within a high-resolution numerical simulation of the North Atlantic Ocean. *J. Geophys. Res.*, **109**, C01003, doi:10.1029/2003JC001770.
- Saunders, P. M., 1973: The instability of a baroclinic vortex. *J. Phys. Oceanogr.*, **3**, 61–65.
- Schmitz, W. J., Jr., cited 2003: On the circulation in and around the Gulf of Mexico. Vol. I: A review of the deep water circulation. [Available online at <http://www.cbi.tamucc.edu/gomcirculation/>]
- Shay, L. K., A. J. Mariano, S. D. Jacob, and E. H. Ryan, 1998: Mean and near-inertial ocean current response to Hurricane Gilbert. *J. Phys. Oceanogr.*, **28**, 858–889.
- Sturges, W., J. C. Evans, S. Welsh, and W. Holland, 1993: Separation of warm core rings in the Gulf of Mexico. *J. Phys. Oceanogr.*, **23**, 250–286.
- Thierry, V., and Y. Morel, 1999: Influence of a strong bottom slope on the evolution of a surface-intensified vortex. *J. Phys. Oceanogr.*, **29**, 911–924.
- Vandermeirsch, F., Y. Morel, and G. Sutyrin, 2001: The net advective effect of a vertically sheared current on a coherent vortex. *J. Phys. Oceanogr.*, **31**, 2210–2225.
- Vukovich, F. M., and G. A. Maul, 1985: Cyclonic eddies in the eastern Gulf of Mexico. *J. Phys. Oceanogr.*, **15**, 105–117.
- , B. W. Crissman, M. Bushnell, and W. J. King, 1979: Some aspects of the Gulf of Mexico using satellite data and in-situ data. *J. Phys. Oceanogr.*, **9**, 1214–1222.
- Wallcraft, A., 1985: Gulf of Mexico circulation modeling study, year 1. JAYCOR Progress Rep., Minerals Management Service Contract 14-12-0001-30073, Metairie, LA.
- , 1986: Gulf of Mexico circulation modeling study, year 2. JAYCOR Progress Rep., Minerals Management Service Contract 14-12-0001-30073, Metairie, LA.
- Welsh, S. E., 1996: A numerical modeling study of the Gulf of Mexico under present and past environmental conditions. Ph.D. dissertation, Louisiana State University, Baton Rouge, LA, 206 pp.
- , and M. Inoue, 2000: Loop Current rings and the deep circulation in the Gulf of Mexico. *J. Geophys. Res.*, **105**, 16 951–16 959.